ELSEVIER

A two-dimensional self-adaptive *hp* finite element method for the characterization of waveguide discontinuities. Part I: Energy-norm based automatic *hp*-adaptivity

Luis E. García-Castillo [a,*,1,2], David Pardo [b,d], Ignacio Gómez-Revuelto [c], Leszek F. Demkowicz [d]

[a] *Departamento de Teoría de la Señal y Comunicaciones, Universidad Carlos III de Madrid, Escuela Politécnica Superior (Edificio Torres Quevedo), Avda. de la Universidad, 30, 28911 Leganés, Madrid, Spain*
[b] *Department of Petroleum and Geosystems Engineering, University of Texas at Austin, Austin, TX 78712, USA*
[c] *Departamento de Ingeniería Audiovisual y Comunicaciones, Universidad Politécnica de Madrid, Madrid, Spain*
[d] *ICES, University of Texas at Austin, Austin, TX 78712, USA*

Abstract

The accurate analysis and characterization of waveguide discontinuities is an important issue in microwave engineering. In some cases, the discontinuities are an unavoidable result of mechanical or electric transitions which effects have to be minimized; in other cases, the discontinuities are deliberately introduced into the waveguide to perform a certain electric function.

This is the first of two papers analyzing different types of rectangular waveguide discontinuities by using a fully automatic *hp*-adaptive finite element method. In this paper, a fully automatic energy-norm based *hp*-adaptive Finite Element (FE) strategy applied to a number of relevant waveguide structures, is presented. The methodology produces exponential convergence rates in terms of the energy-norm error of the solution against the problem size (number of degrees of freedom).

Extensive numerical results demonstrate the suitability of the *hp*-method for solving different rectangular waveguide discontinuities. These results illustrate the flexibility, reliability, and high-accuracy of the method.

The self-adaptive *hp*-FEM provides similar (sometimes more) accurate results than those obtained with semi-analytical techniques such as the mode matching method, for problems where semi-analytical methods can be applied. At the same time, the *hp*-FEM provides the flexibility of modeling more complex waveguide structures and including the effects of dielectrics, metallic screws, round corners, etc., which cannot be easily considered when using semi-analytical techniques.

In the second part, the work is extended by presenting a fully automatic goal-oriented *hp*-adaptive FE in terms of the scattering or S-parameters which are widely used in microwave engineering for the characterization of microwave devices.
© 2007 Elsevier B.V. All rights reserved.

Keywords: Finite element method; *hp*-Adaptivity; Energy-norm; Rectangular waveguides; Waveguide discontinuities; S-parameters

---

1. Introduction

The accurate analysis and characterization of waveguide "discontinuities" is an important issue in microwave engineering (see e.g., [1,2]). A waveguide discontinuity is defined as any interruption in the translational symmetry of the waveguide. In some cases, the discontinuities are

an unavoidable result of mechanical defects in the waveguide, or mechanical and/or electric transitions between two or more waveguides. In these cases, the discontinuity effect is unwanted and its design is focused on minimizing the effect of the discontinuity. This is the case of structures as bends, transitions, junctions, etc., where the goal is to achieve very low levels of energy reflected at the discontinuities. Other waveguides discontinuities are deliberately introduced into the waveguide (producing significant levels of energy reflected at the discontinuities) in order to perform a certain electric function (e.g., posts, iris, stubs, etc.). Furthermore, these type of discontinuities are typically combined in order to perform a more sophisticated function as impedance matching and frequency filtering networks. Thus, the characterization of these microwave engineering devices implies also the analysis of "waveguide discontinuities".

Among the different waveguide technologies encountered in the modern communication systems, the rectangular waveguide technology is used in many of them; in particular, in satellite systems and general communication systems working in the upper microwave and millimeter wave frequency bands. This is due to the simplicity of the geometry, low losses and capacity to handle high powers that characterize the rectangular waveguides.

Within this context, the objective of this work is to analyze rectangular waveguide discontinuities by means of a fully automatic *hp*-adaptive finite element method. The analysis of a general discontinuity problem means to deal with a problem domain as the one shown in Fig. 1. It consists of a region, which may have an arbitrary geometry and several materials inside, and a number of waveguides (i.e., structures with translational symmetry) through which the energy transfer (inwards and outwards) takes place. Thus, the "ports" of the structure are the apertures located at the end of the waveguides. Actually, the structure shown in Fig. 1 is so general that can describe any microwave passive device. In many cases, the geometry of the region is of the same type as the geometry of the waveguides used for the ports, and the problem is known in microwave engineering as a discontinuity problem. A rectangular waveguide discontinuity is a particular case in which the waveguides are rectangular. In practice, many rectangular waveguide discontinuities are invariant along one direction, and the analysis of those structures may be performed in two-dimensions (2D) by simply considering as the problem domain the intersection of the structure with a plane transverse to the invariant direction. This is the case of the so called *H*-plane and *E*-plane rectangular waveguide discontinuities, depending if the plane transverse to the invariant direction is the one that contains the magnetic or the electric field, respectively. More precisely, the objective of this work is the 2D analysis of these *H*-plane and *E*-plane discontinuities. Several examples of discontinuities that fit into this categories are shown in Fig. 2. Results for some of them are included in this paper.

Typically, a microwave engineer is interested in the characterization of the structure in terms of its *scattering parameters* (*S*-parameters or *S*-matrix). That requires the solution of the Maxwell equations within the structure under certain excitations and terminations at the ports, and the evaluation of the *power waves* a_i and b_i, whose physical meaning will be explained later. Also, the microwave engineer may be interested in the field solution in certain regions in order to introduce modifications in the structure. Therefore, the analysis of the discontinuities must include the computation of the *S* parameters.

Due to the extent and nature of the work in this area, the work is presented in two parts. In the first one, the
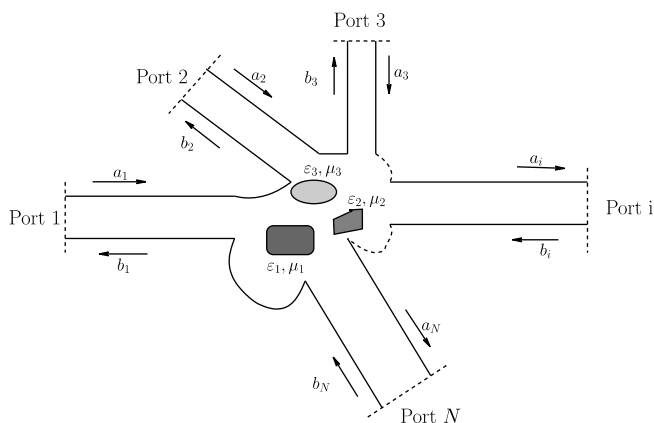

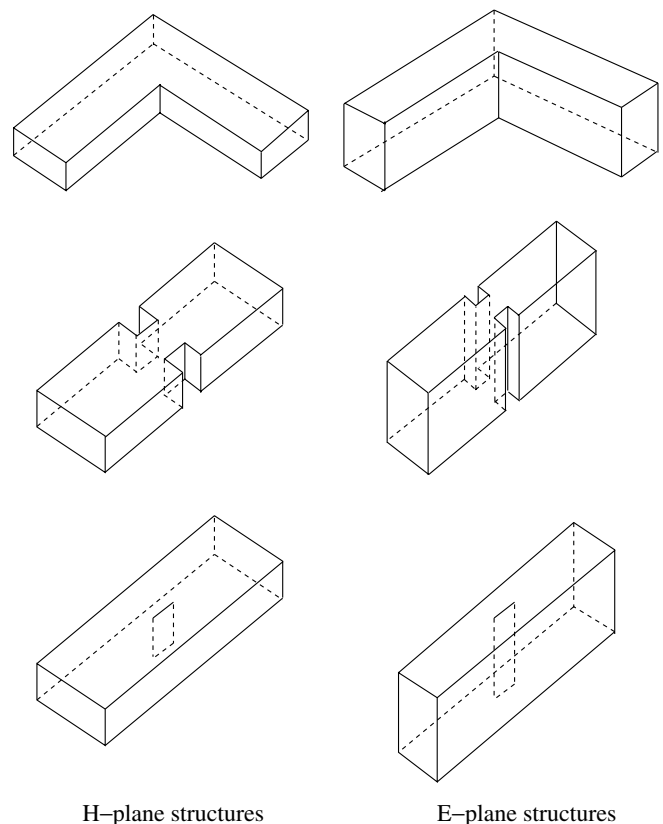Fig. 1. General waveguide discontinuity.

Fig. 2. Examples of *H*-plane and *E*-plane discontinuities.

H-plane and *E*-plane formulations, including stabilized variational formulations for both cases, are presented. We also describe a practical approach for computing scattering parameters using Finite Elements. A numerical methodology based on a self-adaptive *hp*-Finite Element Method [3,4] is used. An implementation for general 2D and 3D electromagnetic problems has been developed by the authors during the last years (see [4–11], for details). In this work, focus on the particular case of *E*-plane and *H*-plane waveguide discontinuity problems is made. Specific formulations corresponding to this class of problems are described. Numerical simulations are performed being the first time the developed *hp*-finite elements and adaptivity is applied to waveguide discontinuity problems of microwave communication systems. Extensive numerical results illustrate the flexibility, reliability and high-accuracy simulations obtained with this methodology, delivering more accurate results than those obtained with semi-analytical (in particular, Mode-Matching [12], [13, Chapter 9]) techniques. The presented numerical results include computation of the *scattering parameters* of the structures. The adaptive methodology has a number of advantages that makes it suitable for the analysis of complex structures (containing several waveguide sections, discontinuities, complex geometries, dielectrics, etc.) in contrast to other semi-analytic and numerical techniques. Namely:

- It automatically resolves different types of singularities i.e., different types of discontinuities.
- It efficiently deals with high frequencies, that is, it delivers a low dispersion error [14,15].
- It provides high-accuracy results, so the S-parameters can be accurately computed.
- It enables modeling of complex (non-uniform) geometries.

In the second paper [16], results obtained using *hp* energy-norm adaptivity [11] are compared against those using a goal-oriented *hp*-adaptivity approach [17–19]. Results show that both methods are suitable for simulation of waveguide discontinuities.

The organization of the paper is as follows. The discontinuity problem in rectangular waveguide technology is introduced in Section 2, where the mathematical formulations for the *H*-plane (Section 2.2.1) and *E*-plane (Section 2.2.2) cases are derived. Stabilized variational formulations for both cases are presented. Procedures to compute the scattering parameters of the structure are described in Section 2.3. The *hp* finite element discretization and automatic adaptivity strategy are briefly described in Sections 3.1 and 3.2, respectively. The refinement strategy is based on the minimization of the *projection based interpolation* error, which is defined in Section 3.2.1. The steps of the mesh optimization algorithm are described in Section 3.2.2. Extensive numerical results, both for the *E*-plane and *H*-plane simulations, are shown in Section 4. Finally, some conclusions are given in Section 5.

2. Analysis of rectangular waveguide discontinuities

As mentioned in the Introduction, the objective of the paper is to analyze the scattering properties of rectangular waveguide discontinuities. A comprehensive approach to this problem requires a basic understanding of guided waves, i.e., "waveguide modes", and, specifically, with rectangular cross-section waveguides. Due to space restrictions, an introduction to the theory of guided waves has been omitted. The reader not familiar with this topic is encouraged to read any of the numerous books in the subject (e.g., [20–24]).

The problem domain of a general discontinuity problem may be thought as a region, which may have arbitrary geometry and several materials inside, and a number of waveguides (i.e., structures with translational symmetry) through which the energy transfer (inwards and outwards the region) takes place. Thus, the waveguides, and more precisely the apertures at the end of the waveguides, are the ports of the structure (Fig. 1). A rectangular waveguide discontinuity is a particular case of a waveguide discontinuity (abstractly represented in Fig. 1) in which the ports are rectangular waveguides. The rectangular waveguides, as any homogeneous waveguide, support TE ("transverse electric") and TM ("transverse magnetic") modes with respect to the translational symmetry axis (ζ in Fig. 3). Those modes experiment a cut-off effect, i.e., propagation occurs only above a certain non-zero frequency. Typically, the modes are ordered in terms of cut-off frequency f_c in the ascending order. The first mode is referred to as the *fundamental mode*. For $a > b$, the first mode (i.e., the fundamental mode) of a rectangular waveguide is the TE_{10} mode. The expressions for its components are obtained by particularizing the results of Table 1 to TE and $m = 1$, $n = 0$. Note that the field of the TE_{10} mode is on the η-direction, i.e., parallel to the narrow edge of the waveguide.

An example of rectangular discontinuity with two ports is shown in Fig. 4. Let us consider a structure that is excited through the fundamental mode (TE_{10}) at a
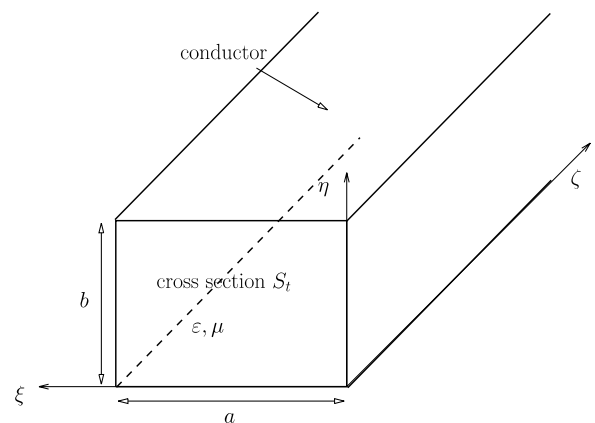

Fig. 3. Rectangular waveguide.

Table 1
Summary of results for the rectangular waveguide

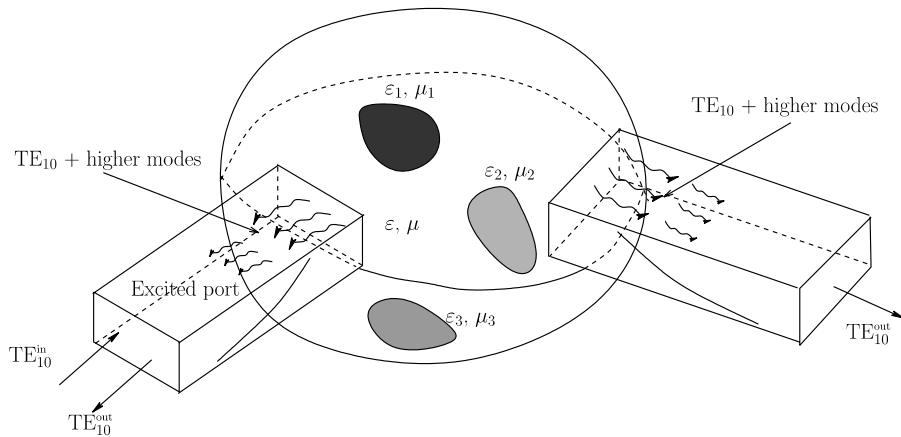| Quantity	TE_{mn}	TM_{mn}
k	$\omega\sqrt{\varepsilon\mu}$	$\omega\sqrt{\varepsilon\mu}$
k_{c}	$\sqrt{\left(\dfrac{m\pi}{a}\right)^2 + \left(\dfrac{n\pi}{b}\right)^2}$	$\sqrt{\left(\dfrac{m\pi}{a}\right)^2 + \left(\dfrac{n\pi}{b}\right)^2}$
β	$\sqrt{k^2 - k_{\mathrm{c}}^2}$	$\sqrt{k^2 - k_{\mathrm{c}}^2}$
E_ζ	0	$B_{mn}\sin\dfrac{m\pi\xi}{a}\sin\dfrac{n\pi\eta}{b}\mathrm{e}^{-\mathrm{j}\beta z}$
H_ζ	$A_{mn}\cos\dfrac{m\pi\xi}{a}\cos\dfrac{n\pi\eta}{b}\mathrm{e}^{-\mathrm{j}\beta z}$	0
E_ξ	$\dfrac{\mathrm{j}\omega\mu n\pi}{k_{\mathrm{c}}^2 b}A_{mn}\cos\dfrac{m\pi\xi}{a}\sin\dfrac{n\pi\eta}{b}\mathrm{e}^{-\mathrm{j}\beta z}$	$\dfrac{-\mathrm{j}\beta m\pi}{k_{\mathrm{c}}^2 a}B_{mn}\cos\dfrac{m\pi\xi}{a}\sin\dfrac{n\pi\eta}{b}\mathrm{e}^{-\mathrm{j}\beta z}$
E_η	$\dfrac{-\mathrm{j}\omega\mu m\pi}{k_{\mathrm{c}}^2 a}A_{mn}\sin\dfrac{m\pi\xi}{a}\cos\dfrac{n\pi\eta}{b}\mathrm{e}^{-\mathrm{j}\beta z}$	$\dfrac{-\mathrm{j}\beta n\pi}{k_{\mathrm{c}}^2 b}B_{mn}\sin\dfrac{m\pi\xi}{a}\cos\dfrac{n\pi\eta}{b}\mathrm{e}^{-\mathrm{j}\beta z}$
H_ξ	$\dfrac{\mathrm{j}\beta m\pi}{k_{\mathrm{c}}^2 a}A_{mn}\sin\dfrac{m\pi\xi}{a}\cos\dfrac{n\pi\eta}{b}\mathrm{e}^{-\mathrm{j}\beta z}$	$\dfrac{\mathrm{j}\omega\varepsilon n\pi}{k_{\mathrm{c}}^2 b}B_{mn}\sin\dfrac{m\pi\xi}{a}\cos\dfrac{n\pi\eta}{b}\mathrm{e}^{-\mathrm{j}\beta z}$
H_η	$\dfrac{\mathrm{j}\beta n\pi}{k_{\mathrm{c}}^2 b}A_{mn}\cos\dfrac{m\pi\xi}{a}\sin\dfrac{n\pi\eta}{b}\mathrm{e}^{-\mathrm{j}\beta z}$	$\dfrac{-\mathrm{j}\omega\varepsilon m\pi}{k_{\mathrm{c}}^2 a}B_{mn}\cos\dfrac{m\pi\xi}{a}\sin\dfrac{n\pi\eta}{b}\mathrm{e}^{-\mathrm{j}\beta z}$
Z	$Z_{\mathrm{TE}} = \dfrac{\omega\mu}{\beta}$	$Z_{\mathrm{TM}} = \dfrac{\beta}{\omega\varepsilon}$

Fig. 4. Example of 2-ports monomode rectangular waveguide discontinuity.

given port. The fundamental mode satisfies the Maxwell equations and the boundary conditions for the waveguide. However, at the discontinuity, the field solution is no longer equal to the TE_{10} mode as this mode does not satisfy, in general, the boundary conditions in this region. The field solution in the discontinuity region will generate, in general, all the modes in the waveguides of the structure going outwards the region in order for the boundary conditions to be satisfied. Thus, part of the energy is reflected back into the excited port and the rest of the energy is transmitted to the other ports. If the frequency of the time-harmonic excitation is within the

monomode region (below the cutoff frequency of the second mode) the field amplitude of all the modes but the TE_{10} will be negligible in the waveguides at a certain distance from the discontinuity region (for practical purposes, one TE_{10} wavelength or even less is usually enough). Thus, at the ports of the structure, only the TE_{10} mode is present. The discontinuity is simply characterized by the ratio of power carried by the reflected TE_{10} wave (for the excited port) or by the transmitted TE_{10} wave (for the other ports) to power carried by the incident TE_{10} wave (at the incident port). These ratios are directly related to the so-called *scattering matrix* or *S-parameters*. They will be rigorously defined later.

2.1. Analysis of waveguide discontinuities in 2D

In the general case, a 3D analysis is needed to obtain the electromagnetic field of the waveguide discontinuity under analysis. However, most commonly, the geometry of the discontinuity is invariant along a transverse direction. Thus, the spatial variation of the fields in the discontinuity along that direction is known (equal to the variation of the field of the incident mode at the discontinuity along that invariant direction) and the scattering analysis may be done in 2D. This is the case of the so-called *H*-plane and *E*-plane rectangular waveguide discontinuities. A large number of bends, junctions, phase shifters, filters, etc. in rectangular technology (see the examples of Fig. 2) fit into this category.

A rectangular *H*-plane discontinuity (see Fig. 5) has translational symmetry along the narrow dimension of the waveguide (the η-axis in Fig. 3). In this case, the FEM analysis may be made by considering as the problem domain the intersection of a plane orthogonal to η with the structure under analysis. That plane is the one containing the magnetic field of the TE_{10}, and the analysis is made in the *H-plane* of the structure. Analogously, in a rectangular *E*-plane discontinuity (see Fig. 6) there is translational symmetry along the broad dimension of the waveguide (the ξ-axis in Fig. 3). In this case, the FEM analysis may be made by considering as the problem domain the intersection of a plane orthogonal to ξ with the structure under analysis. That plane contains the electric field of the TE_{10}, and the analysis is made in the *E-plane* of the structure.

2.2. 2D variational formulation

The 2D variational formulation for the *H*-plane and *E*-plane discontinuity problems are developed next. In both cases, the formulations are based on decomposing the electric and magnetic fields in terms of their components parallel to the *H*-plane $\mathbf{H}_{\Omega}$ (or *E*-plane $\mathbf{E}_{\Omega}$), and orthogonal to it $\mathbf{H}_{\perp}$ (or $\mathbf{E}_{\perp}$). Doing the same with the differential operator ∇ (i.e., $\nabla = \nabla_{\Omega} + \nabla_{\perp}$), Maxwell's curl equations are written as (for the time harmonic case):

$$(\nabla_{\Omega} \times \mathbf{E}_{\perp}) + (\nabla_{\perp} \times \mathbf{E}_{\Omega}) = -j\omega\mu\mathbf{H}_{\Omega}, \tag{1}$$

$$(\nabla_{\Omega} \times \mathbf{E}_{\Omega}) = -j\omega\mu\mathbf{H}_{\perp}, \tag{2}$$

$$(\nabla_{\Omega} \times \mathbf{H}_{\perp}) + (\nabla_{\perp} \times \mathbf{H}_{\Omega}) = j\omega\varepsilon\mathbf{E}_{\Omega}, \tag{3}$$

$$(\nabla_{\Omega} \times \mathbf{H}_{\Omega}) = j\omega\varepsilon\mathbf{E}_{\perp} \tag{4}$$

being the unknowns complex valued *phasors* corresponding to field amplitudes. The symbols ε and μ stand for the electric permittivity and magnetic permeability, respectively, and ω is the angular frequency. Particularization to each case (*H*-plane or *E*-plane) is shown next.

2.2.1. H-plane variational formulation

In the *H*-plane discontinuities, the variation along the orthogonal direction to the plane, i.e., along the narrow dimension of the waveguide, is null for TE_{10} mode excitation. Thus, $\nabla_{\perp} \equiv 0$ and, by combining (1) and (4), a double curl vector wave equation is obtained in term of $\mathbf{H}_{\Omega}$:

$$\nabla \times \frac{1}{\varepsilon} \nabla \times \mathbf{H}_{\Omega} - \omega^2\mu\mathbf{H}_{\Omega} = 0 \tag{5}$$

or, equivalently,

$$\nabla \times \frac{1}{\varepsilon_r} \nabla \times \mathbf{H}_{\Omega} - k_0^2\mu_r\mathbf{H}_{\Omega} = 0, \tag{6}$$

where $\varepsilon_r = \varepsilon/\varepsilon_0$, $\mu_r = \mu/\mu_0$, and $k_0 = \omega\sqrt{\varepsilon_0\mu_0}$.[3] Note that the subindex 0 is used to particularize to vacuum medium. For simplicity, the operator ∇_{Ω} has been simply referred to as ∇. This convention will be kept in the rest of the paper except when explicitly noted.

The boundary conditions are (see Fig. 5):

$$\hat{\mathbf{n}} \times \mathbf{H}_{\Omega} = 0, \quad \text{at perfect magnetic conductors } (\Gamma_D), \tag{7}$$

$$\hat{\mathbf{n}} \times \frac{1}{\varepsilon_r} \nabla \times \mathbf{H}_{\Omega} = 0, \quad \text{at perfect electric conductors } (\Gamma_N), \tag{8}$$

$$\hat{\mathbf{n}} \times \frac{1}{\varepsilon_r} \nabla \times \mathbf{H}_{\Omega} + j\frac{k^2}{\varepsilon_r\beta_{10}}\hat{\mathbf{n}} \times \hat{\mathbf{n}} \times \mathbf{H}_{\Omega} = \mathbf{U}^{in},$$
$$\text{at the port boundaries } (\Gamma_p) \tag{9}$$

with $\mathbf{U}^{in}$ defined as

$$\mathbf{U}^{in} = 2j\frac{k^2}{\varepsilon_r\beta_{10}}\hat{\mathbf{n}} \times \hat{\mathbf{n}} \times \mathbf{H}^{in} \tag{10}$$

and $\mathbf{H}^{in}$ being the magnetic field incident at the port corresponding to the TE_{10} mode. $\hat{\mathbf{n}}$ stands for the outward unit vector normal to Γ.

Perfect magnetic conductors are not present physically in the structure under analysis (neither are shown in Fig. 5) but they may be used in certain cases as symmetry boundary conditions for the FEM analysis, in order to reduce the number of unknowns.

The variational formulation is obtained by multiplying (6) with a test function $\mathbf{F}_{\Omega}$. Integration by parts (first vector

---

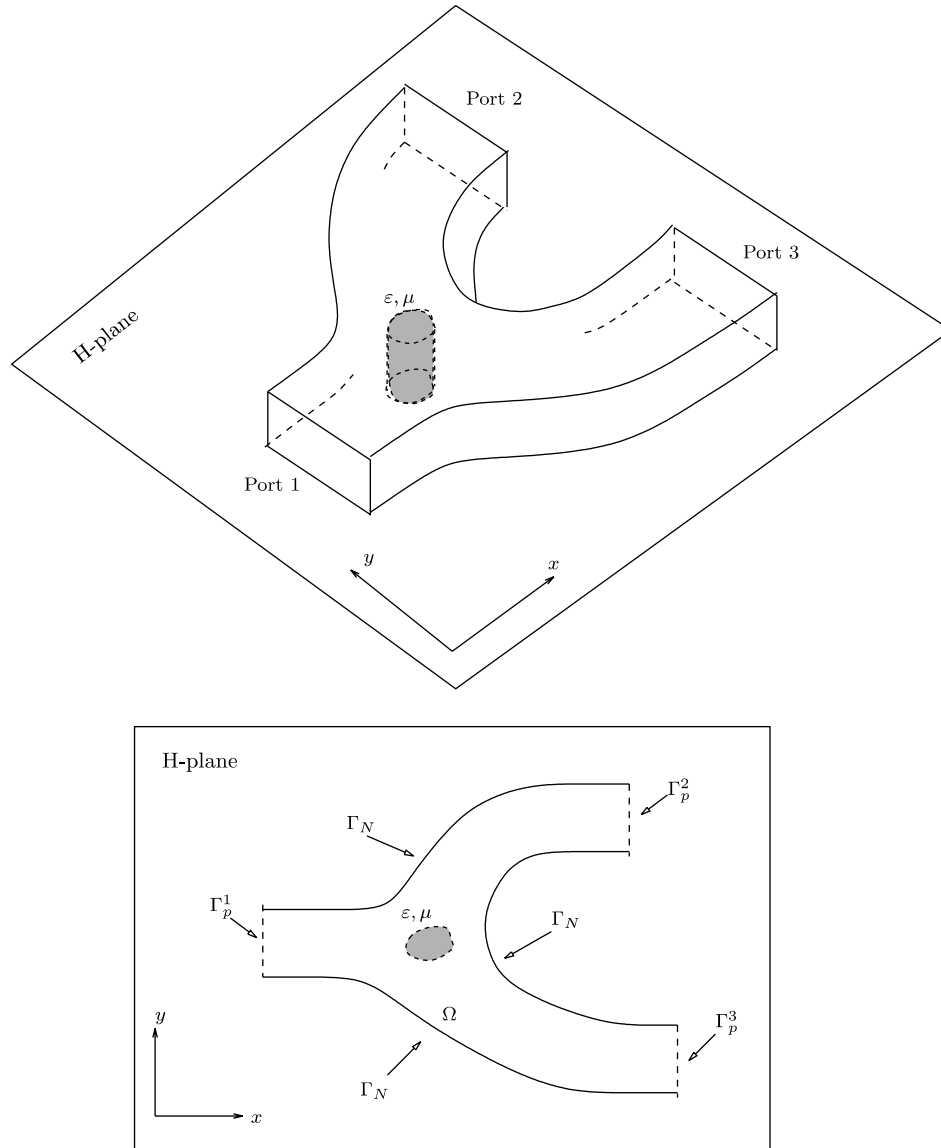[3] In the general case, $k = \omega\sqrt{\varepsilon\mu}$ is the wavenumber.

Fig. 5. A rectangular *H*-plane discontinuity and its 2D FEM modeling.

Green's theorem) is applied to the double curl term and a boundary term appears in the variational formulation:

$$\int_{\Omega} \mathbf{F}_{\Omega} \cdot \left(\nabla \times \frac{1}{\varepsilon_r} \nabla \times \mathbf{H}_{\Omega} \right) d\Omega$$

$$= \int_{\Omega} (\nabla \times \mathbf{F}_{\Omega}) \cdot \left(\frac{1}{\varepsilon_r} \nabla \times \mathbf{H}_{\Omega} \right) d\Omega$$

$$- \int_{\Gamma} \hat{n} \cdot \left(\mathbf{F}_{\Omega} \times \frac{1}{\varepsilon_r} \nabla \times \mathbf{H}_{\Omega} \right) d\Gamma. \tag{11}$$

Let us define the following spaces

$$\mathbf{W} := \{ \mathbf{A} \in \mathbf{H}(\text{curl}, \Omega), \hat{\mathbf{n}} \times \mathbf{A} = 0 \quad \text{on } \Gamma_{\mathrm{D}} \},$$
$$V := \{ p \in H^1(\Omega), p = 0 \quad \text{on } \Gamma_{\mathrm{D}} \}. \tag{12}$$

The boundary term for Γ_{D} is zero by selecting $\mathbf{F}_{\Omega} \in \mathbf{W}$. Also, for Γ_N the boundary term is set to zero in order to

enforce, in a natural sense, (8). Thus, the boundary term is only non-zero at the boundary ports. Introducing (9) in the boundary terms for the ports, the following variational formulation is obtained:

Find $\mathbf{H}_{\Omega} \in \mathbf{W}$ such that

$$c(\mathbf{F}_{\Omega}, \mathbf{H}_{\Omega}) = l(\mathbf{F}_{\Omega}), \quad \forall \mathbf{F}_{\Omega} \in \mathbf{W}, \tag{13}$$

where $c(\mathbf{F}_{\Omega}, \mathbf{H}_{\Omega})$ and $l(\mathbf{F}_{\Omega})$ are defined in (15).

This variational formulation is not uniformly stable with respect to (angular) frequency ω. As $\omega \to 0$, i.e., $k_0 \to 0$, the term $k_0^2 \int_{\Omega} \mathbf{F}_{\Omega} \cdot \mu_r \mathbf{H}_{\Omega} d\Omega$ becomes negligible compared with the curl-product term $\int_{\Omega} (\nabla \times \mathbf{F}_{\Omega}) \cdot \left(\frac{1}{\varepsilon_r} \nabla \times \mathbf{H}_{\Omega} \right) d\Omega$. Thus, for small frequencies the problem becomes ill-posed, since numerically the term with the product of the curls does not "see" the gradients, and the gradients remain undetermined. This situation is not an issue from the prac-
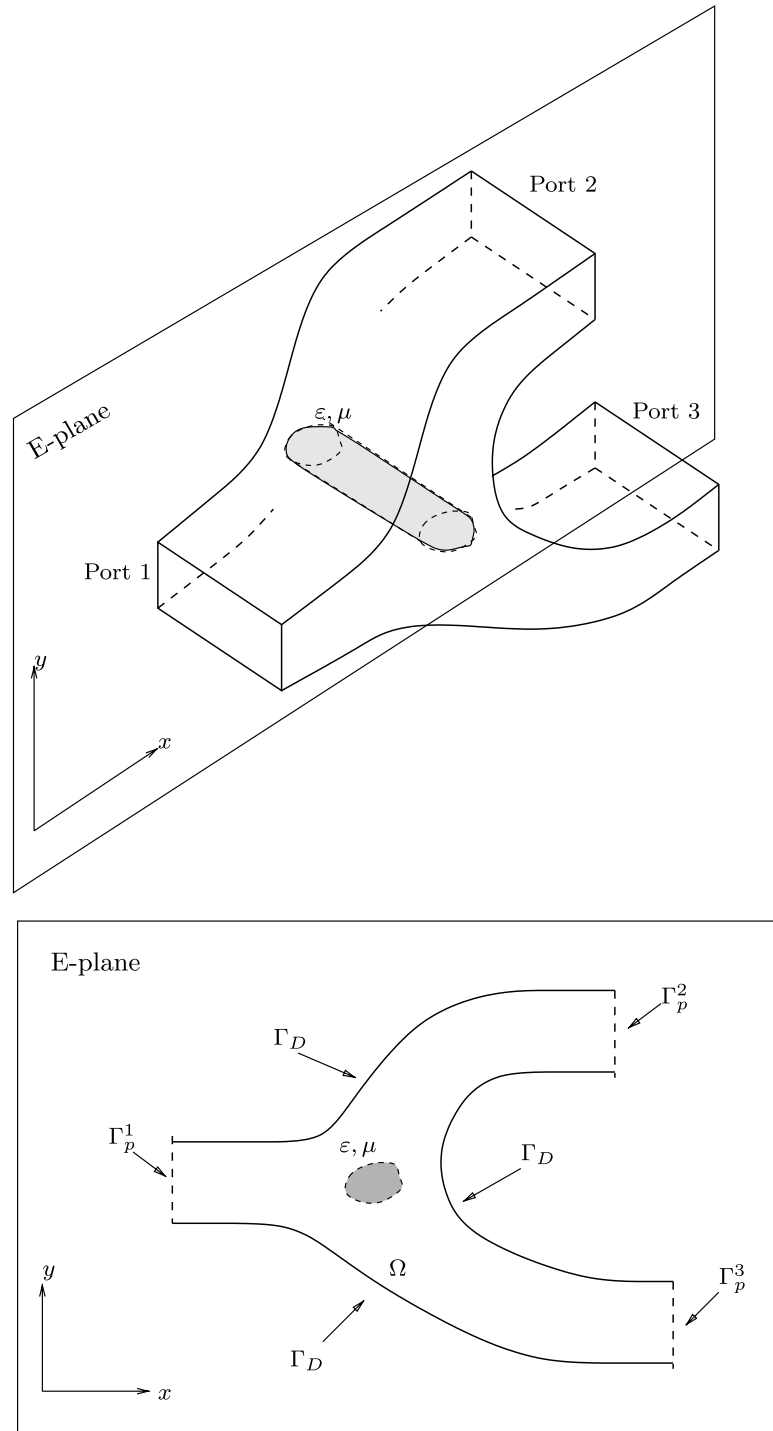
Fig. 6. A rectangular *E*-plane discontinuity and its 2D FEM modeling.

tical point of view for the *H*-plane formulation because, in order for the TE_{10} mode to propagate, k_0 has to be chosen in such a way that $k_0 \varepsilon_r \mu_r > \pi/a$. However, the stability problem may also arise with very small size finite elements as the product of the curls term becomes dominant in the formulation.

As a remedy to this problem, a Lagrange multiplier *p* is introduced to enforce the weak form of the continuity equation (obtained by employing a gradient as a test func-

tion in (13)). Thus, the *stabilized* variational formulation with the Lagrange multiplier is:

Find $\mathbf{H}_\Omega \in \mathbf{W}$, $p \in V$ such that

$$c(\mathbf{F}_\Omega, \mathbf{H}_\Omega) + b(\mathbf{F}_\Omega, \nabla p) = l(\mathbf{F}_\Omega) \quad \forall \mathbf{F}_\Omega \in \mathbf{W}$$
$$b(\nabla q, \mathbf{H}_\Omega) = g(\nabla q) \quad \forall q \in V$$

(14)

The sesquilinear and antilinear forms used in the variational formulations above are the following:

$$c(\mathbf{F}_\Omega, \mathbf{H}_\Omega) = \int_\Omega (\nabla \times \overline{\mathbf{F}}_\Omega) \cdot \left(\frac{1}{\varepsilon_r} \nabla \times \mathbf{H}_\Omega \right) d\Omega$$

$$- k_0^2 \int_\Omega \overline{\mathbf{F}}_\Omega \cdot \mu_r \mathbf{H}_\Omega d\Omega$$

$$+ j \frac{k^2}{\varepsilon_r \beta_{10}} \int_{\sum_i \Gamma_p^i} (\hat{\mathbf{n}} \times \overline{\mathbf{F}}_\Omega) \cdot (\hat{\mathbf{n}} \times \mathbf{H}_\Omega) d\Gamma,$$

$$b(\mathbf{F}_\Omega, \nabla p) = -k_0^2 \int_\Omega \overline{\mathbf{F}}_\Omega \cdot \mu_r \nabla p \, d\Omega \qquad (15)$$

$$+ j \frac{k^2}{\varepsilon_r \beta_{10}} \int_{\sum_i \Gamma_p^i} (\hat{\mathbf{n}} \times \overline{\mathbf{F}}_\Omega) \cdot (\hat{\mathbf{n}} \times \nabla p) d\Gamma,$$

$$l(\mathbf{F}_\Omega) = 2j \frac{k^2}{\varepsilon_r \beta_{10}} \int_{\Gamma_p^{in}} (\hat{\mathbf{n}} \times \overline{\mathbf{F}}_\Omega) \cdot (\hat{\mathbf{n}} \times \mathbf{H}^{in}) d\Gamma,$$

$$g(\nabla q) = 2j \frac{k^2}{\varepsilon_r \beta_{10}} \int_{\Gamma_p^{in}} (\hat{\mathbf{n}} \times \nabla \bar{q}) \cdot (\hat{\mathbf{n}} \times \mathbf{H}^{in}) d\Gamma,$$

where $\overline{\mathbf{F}}$ and $\bar{q}$ stands for the complex conjugate of $\mathbf{F}$ and q, respectively.

By substituting $\mathbf{F}_\Omega = \nabla q, q \in V$, it is deduced that the Lagrange multiplier p satisfies the weak form of a Laplace-like equation. Thus, if (homogeneous) Dirichlet boundary conditions are present ($\Gamma_D \neq \emptyset$), i.e., when symmetry walls are used in the analysis, the Lagrange multiplier p identically vanishes. Notice that the multiplier p is an undefined constant when $\Gamma_D = \emptyset$. In that case, one degree of freedom of p is set to a given value (typically zero). Thus, the multiplier p identically vanishes for $\Gamma_D = \emptyset$. Also, notice that $b(\mathbf{F}_\Omega, \nabla p)$ and $g(\nabla q)$ should both be divided by k_0.

The stabilized formulation works because the gradients of scalar-valued potentials from V form precisely the null space of the curl on vector functions in $\mathbf{H}$. This condition will have to be preserved at the discrete level by a careful construction of the finite element basis [25].

2.2.2. E-plane variational formulation

The E-plane discontinuities analysis is similar to the H-plane case in the sense that the problem domain is restricted to a plane. However, the formulation presents some relevant differences with respect to the one used for the H-plane discontinuities. The reason is that the orthogonal direction to the plane (E-plane) is the broad dimension of the rectangular waveguide and, in contrast to the H-plane case, $\nabla_\perp \neq 0$ for TE$_{10}$ mode excitation.

Thus, by combining (3) and (2), it is obtained

$$\nabla \times \frac{1}{\mu} \nabla \times \mathbf{E}_\Omega + j\omega(\nabla_\perp \times \mathbf{H}_\Omega) - \omega^2 \varepsilon \mathbf{E}_\Omega = 0. \qquad (16)$$

With the local axis convention of Fig. 3, $\nabla_\perp$ corresponds to the derivatives in the ξ-direction (along the broad dimension of the waveguide), which are non-zero for TE$_{10}$ mode excitation, as mentioned above. More precisely, due to the translational symmetry in the orthogonal direction to the E-plane (ξ-direction), the variation along the orthogonal

direction to the E-plane ($\nabla_\perp$) will be of the same type as the TE$_{10}$ mode, i.e., as $\sin(\pi\xi/a)$ or $\cos(\pi\xi/a)$ depending on the vector component of the field. Furthermore, if the discontinuity is homogeneous,[4] it can be inferred that $\mathbf{E}_\perp = 0$ everywhere under TE$_{10}$ mode excitation.

Thus, the double-curl vector wave equation may be written as:

$$\nabla \times \nabla \times \mathbf{E}_\Omega - \beta_{10}^2 \mathbf{E}_\Omega = 0. \qquad (17)$$

It is worth noting that the above wave equation is not valid for the analysis of E-plane inhomogeneous structures, which requires, in the general case, the three components of the electric field [26,27]. The wave equation of (17) in terms of two components (vector $\mathbf{E}_\Omega$) has been used for comparison purposes with the formulation based on (6) used for the H-plane case.

The boundary conditions of the problem are (see Fig. 6):

$$\hat{\mathbf{n}} \times \mathbf{E}_\Omega = 0, \quad \text{at perfect electric conductors } (\Gamma_D), \qquad (18)$$

$$\hat{\mathbf{n}} \nabla \times \mathbf{E}_\Omega = 0, \quad \text{at perfect magnetic conductors } (\Gamma_N), \qquad (19)$$

$$\hat{\mathbf{n}} \times \nabla \times \mathbf{E}_\Omega + j\beta_{10}\hat{\mathbf{n}} \times \hat{\mathbf{n}} \times \mathbf{E}_\Omega = \mathbf{U}^{in},$$

$$\text{at the port boundaries } (\Gamma_p) \qquad (20)$$

with $\mathbf{U}^{in}$ defined as

$$\mathbf{U}^{in} = 2j\beta_{10}\hat{\mathbf{n}} \times \hat{\mathbf{n}} \times \mathbf{E}^{in} \qquad (21)$$

and $\mathbf{E}^{in}$ being the electric field incident at the port corresponding to the TE$_{10}$ mode. $\hat{\mathbf{n}}$ stands for the outward unit vector normal to Γ. The symbol β_{10} stands for the propagation constant (see Table 1) for the TE$_{10}$ mode.

Analogous remarks with respect to the validity of the boundary conditions at the ports made in the H-plane case hold in the E-plane.

The variational formulation for the E-plane is the following.

Find $\mathbf{E}_\Omega \in \mathbf{W}$ such that

$$c(\mathbf{F}_\Omega, \mathbf{E}_\Omega) = l(\mathbf{F}_\Omega), \quad \forall \mathbf{F}_\Omega \in \mathbf{W}, \qquad (22)$$

where $c(\mathbf{F}_\Omega, \mathbf{E}_\Omega)$ and $l(\mathbf{F}_\Omega)$ are defined in (24).

Analogously to the H-plane formulation of (13), formulation (22) is not uniformly stable with respect to β_{10}. There is a significant difference with respect to the H-plane formulation. In (22), the constant in front of the integral term of the product of the test and trial (unknown) functions (i.e., β_{10}^2) may be chosen arbitrarily close to zero in the region where the TE$_{10}$ mode still propagates. The physical meaning of selecting $\beta_{10} \to 0$ is that the frequency is chosen very close to cut-off. In other words, the wavelength is very close to infinity and the problems of scales due to the ratio of the finite element size to the wavelength in the double

---

[4] A homogeneous discontinuity is defined as a discontinuity with only one material filling the discontinuity. Note that the presence of perfect (electric or magnetic) conductors does not alter the homogeneous character of the discontinuity, since the electromagnetic field is null inside perfect conductors. Thus, the definition of only one material stands for the regions where the electromagnetic field is non-null.

curl formulation arises, even with "reasonable" size finite elements.

As a remedy to this problem, a Lagrange multiplier p is introduced to enforce the weak form of the continuity equation (obtained by employing a gradient as test function in (22)). Thus, the *stabilized* variational formulation with the Lagrange multiplier, in the *E*-plane case, is obtained:

Find $\mathbf{E}_\Omega \in \mathbf{W}$, $p \in V$ such that

$$c(\mathbf{F}_\Omega, \mathbf{E}_\Omega) + b(\mathbf{F}_\Omega, \nabla p) = l(\mathbf{F}_\Omega) \quad \forall \mathbf{F}_\Omega \in \mathbf{W},$$
$$b(\nabla q, \mathbf{E}_\Omega) = g(\nabla q) \quad \forall q \in V. \tag{23}$$

The sesquilinear and antilinear forms used in the variational formulations above are as follows:

$$c(\mathbf{F}_\Omega, \mathbf{E}_\Omega) = \int_\Omega (\nabla \times \overline{\mathbf{F}}_\Omega) \cdot (\nabla \times \mathbf{E}_\Omega) d\Omega - \beta_{10}^2 \int_\Omega \overline{\mathbf{F}}_\Omega \cdot \mathbf{E}_\Omega \, d\Omega$$
$$+ j\beta_{10} \int_{\sum_i \Gamma_p^i} (\hat{\mathbf{n}} \times \overline{\mathbf{F}}_\Omega) \cdot (\hat{\mathbf{n}} \times \mathbf{E}_\Omega) d\Gamma,$$

$$b(\mathbf{F}_\Omega, \nabla p) = -\beta_{10}^2 \int_\Omega \overline{\mathbf{F}}_\Omega \cdot \nabla p \, d\Omega$$
$$+ j\beta_{10} \int_{\sum_i \Gamma_p^i} (\hat{\mathbf{n}} \times \overline{\mathbf{F}}_\Omega) \cdot (\hat{\mathbf{n}} \times \nabla p) d\Gamma,$$

$$l(\mathbf{F}_\Omega) = 2j\beta_{10} \int_{\Gamma_p^{\mathrm{in}}} (\hat{\mathbf{n}} \times \overline{\mathbf{F}}_\Omega) \cdot (\hat{\mathbf{n}} \times \mathbf{E}^{\mathrm{in}}) d\Gamma,$$

$$g(\nabla q) = 2j\beta_{10} \int_{\Gamma_p^{\mathrm{in}}} (\hat{\mathbf{n}} \times \nabla \overline{q}) \cdot (\hat{\mathbf{n}} \times \mathbf{E}^{\mathrm{in}}) d\Gamma. \tag{24}$$

By substituting $\mathbf{F}_\Omega = \nabla q, q \in V$, it is deduced that the Lagrange multiplier p satisfies the weak form of a Laplace-like equation. In the *E*-plane case, in contrast to the *H*-plane case, (homogeneous) Dirichlet boundary conditions are always present ($\Gamma_D \neq 0$) because of the presence of the conductors. Thus, the multiplier p identically vanishes.

Note that $b(\mathbf{F}, \nabla p)$ and $g(\nabla q)$ should both be divided by β_{10}.

2.3. Computation of scattering parameters

A discontinuity (actually, any *N*-port microwave network) may be characterized by the so called *scattering matrix S*. Provided that only one mode is propagating in the waveguide ports, the field at a given port, in the general case, will consist of the contributions of two waves: one going inward and the other going outward the port. Each of these waves is defined by a complex-valued magnitude called *power wave*. For its definition in terms of circuit magnitudes (voltages and currents), the reader is referred to [28] or a microwave theory textbook (e.g., [23]). For understanding what follows, it is enough to know that the power wave is a complex number such that its square magnitude is the power carried by the wave, and its argument is the phase of the wave. At each port Γ_p^i the power

wave going inward is denoted as a_i and the one going outward b_i. Thus, a_i will be proportional to H_0^{in} or E_0^{in}, and b_i will be proportional to H_0^{out} or E_0^{out} (being H_0^{in}, E_0^{in} and H_0^{out}, E_0^{out} the amplitudes of the inward and outward waves, respectively). Therefore, it is easy to infer that the relation between the power waves is linear (for linear media). These linear relations may be casted into matrix form as follows

$$\begin{Bmatrix} b_1 \\ b_2 \\ . \\ . \\ b_N \end{Bmatrix} = \begin{bmatrix} S_{11} & S_{12} & \ldots & S_{1N} \\ S_{21} & S_{22} & \ldots & S_{2N} \\ . & . & \ldots & . \\ . & . & \ldots & . \\ S_{N1} & S_{N2} & \ldots & S_{NN} \end{bmatrix} \begin{Bmatrix} a_1 \\ a_2 \\ . \\ . \\ a_N \end{Bmatrix}, \tag{25}$$

where S_{ij} are the so-called scattering parameters, or simply *S* parameters. Note that S_{ii} are reflection coefficients and $S_{ji}, j \neq i$, are transmission coefficients.

Expression (25) completely determines the electrical behavior of the network when only one mode is present (with non-negligible level) at the ports.[5] The *S* matrix is symmetric if and only if the circuit is reciprocal.[6] This is the case of the structures analyzed in this paper. Non-reciprocal behavior would require a non-symmetric tensor for the electric permittivity and/or magnetic permeability. For a lossless structure the *S* matrix is unitary.

Typically, the *S* parameters are obtained by making N "measurements". At each measurement i, the port Γ_p^i is excited ($a_i \neq 0$, $\Gamma_p^i \equiv \Gamma_p^{\mathrm{in}}$) and the others are "adapted", i.e., no reflection back into the circuit occurs ($a_j = 0$, $j \neq i$). Thus, the coefficients on the i column ($i = 1, \ldots, N$) of the *S* parameters matrix are obtained as

$$S_{ji} = b_j/a_i, \quad j = 1, \ldots, N, \tag{26}$$

Obviously, the knowledge of some properties of the structure under analysis (reciprocal or not, lossless or lossy, the presence of some symmetries, etc.) allows to infer some of the *S* parameters in terms of others, so the *S* matrix may be obtained with a lower number of experiments.

When the analysis is made in the computer, each of the "measurements" correspond to the assumption that there is a given incident field (inward to the structure) at a given port and zero incident field in the other ports. In order for the analysis to be meaningful, the ports must absorb the waves, so no reflection is produced by truncating the waveguides for the simulation. This condition is known in the microwave literature as an "adaptation" condition and is achieved by absorbing boundary conditions at the ports (as those of (9) and 20).[7]

---

[5] A multimode *S* matrix may be obtained by writing the linear relations between the power waves of the ports for the different modes if needed.

[6] In the simplest sense, a reciprocal system is such that the response of the system to a source is interchanged when source and measurer are interchanged. It can be demonstrated that any system in which the media are linear with permittivity and permeability characterized (in the general case) by symmetric tensors is reciprocal.

[7] Multimode boundary conditions may also be used for this purpose.

Once the magnetic and/or electric field is known within the structure, and, in particular, its tangential component to each port, the S parameters may be computed as ratios of power waves (Eq. (26)).

The transverse component of the field at the excited port Γ_p^i is given by the sum of contributions of two TE_{10} waves (one inward – incident – and the other outward – reflected –):

$$\mathbf{V}_t^{p_i}(\xi, \eta) = a_i \mathbf{v}_{10}^{p_i}(\xi, \eta) + b_i \mathbf{v}_{10}^{p_i}(\xi, \eta), \tag{27}$$

where $\mathbf{v}_{10}^{p_i}(\xi, \eta)$ is a real-valued vector function that represents the "shape" of the field at the port.

It may be easily shown that $\mathbf{v}_{10}^{p_i}(\xi, \eta)$[8] is proportional to $\sin(\pi\xi/a)$, being a the broad dimension of the waveguide at port i. Also, it is obvious that, as it was mentioned before, a_i is proportional to the phasor of the inward wave and b_i is proportional to the phasor of the outward wave. On the following, V_0^{in} will be used indistinctly to refer to the magnetic or electric field amplitude (phasor) of the inward wave. Analogously, V_0^{out} will be used to refer to the outward wave.

Normalization of $\mathbf{v}_{10}^{p_i}(\xi, \eta)$ is obtained by enforcing the power wave definition, i.e., the power of the wave is given by $|a_i|^2$, or $|b_i|^2$, accordingly. Thus,

$$\mathbf{v}_{10}^{p_i}(\xi, \eta) = \sqrt{\frac{2I_{10}^{p_i}}{a^{p_i} b^{p_i}}} \sin \frac{\pi\xi}{a^{p_i}} \hat{\mathbf{a}}_\xi \tag{28}$$

and

$$a_i = V_0^{\text{in}} \sqrt{\frac{a^{p_i} b^{p_i}}{2I_{10}^{p_i}}}, \quad b_i = V_0^{\text{out}} \sqrt{\frac{a^{p_i} b^{p_i}}{2I_{10}^{p_i}}}. \tag{29}$$

Multiplying (27) by $\mathbf{v}_{10}^{p_i}(\xi, \eta)$ and integrating over the cross-section of the rectangular waveguide corresponding to the ith port, $S_t^{p_i}$, we get (after several manipulations):

$$S_{ii} = \frac{\frac{1}{I_{10}^{p_i}} \int_{S_t^{p_i}} \mathbf{V}_t^{p_i}(\xi, \eta) \cdot \mathbf{v}_{10}^{p_i}(\xi, \eta) \mathrm{d}S_t^{p_i}}{V_0^{\text{in}} \sqrt{\frac{a^{p_i} b^{p_i}}{2I_{10}^{p_i}}}} - 1, \tag{30}$$

where $I_{10}^{p_i}$ defines an *inmittance* such as $I_{10}^{p_i} = Z_{\text{TE}_{10}}^{p_i}$ with $\mathbf{V}_t \equiv \mathbf{E}_t$ and $I_{10}^{p_i} = 1/Z_{\text{TE}_{10}}^{p_i}$ with $\mathbf{V}_t \equiv \mathbf{H}_t$.

For H- and E-plane structures, the integral over the cross-section can be made analytically along one of the axis of the ports as the variation of the field along that given direction is known. Taking into account (28) and (29), the expression (30) for the reflection coefficient S_{ii} is simplified as follows:

$$S_{ii} = \frac{\int_{\Gamma_{p_i}} \mathbf{H}_\Omega(\xi) \cdot \sin \frac{\pi\xi}{a^{p_i}} \mathrm{d}\boldsymbol{\Gamma}_{p_i}}{H_0^{\text{in}} \frac{a^{p_i}}{2}} - 1 \quad (H\text{-plane}) \tag{31}$$

$$S_{ii} = \frac{\int_{\Gamma_{p_i}} \mathbf{E}_\Omega(\eta) \cdot \mathrm{d}\boldsymbol{\Gamma}_{p_i}}{E_0^{\text{in}} b^{p_i}} - 1 \quad (E\text{-plane}) \tag{32}$$

---

[8] Actually, for the TE_{10} mode, $\mathbf{v}_{10}$ is not a function of η, i.e., $\mathbf{v}_{10}(\xi, \eta) \equiv \mathbf{v}_{10}(\xi)$.

The procedure to obtain the expression for $S_{ji}(j \neq i)$ is analogous. Considering (27) for the jth port with only an outward wave (i.e., $a_j = 0$), and multiplying by $\mathbf{v}_{10}^{p_j}(\xi, \eta)$ and integrating over $S_t^{p_j}$, S_{ji} is finally obtained as:

$$S_{ji} = \frac{\frac{1}{I_{10}^{p_j}} \int_{S_t^{p_j}} \mathbf{V}_t^{p_j}(\xi, \eta) \cdot \mathbf{v}_{10}^{p_j}(\xi, \eta) \mathrm{d}S_t^{p_j}}{V_0^{\text{in}} \sqrt{\frac{a^{p_i} b^{p_i}}{2I_{10}^{p_i}}}}, \tag{33}$$

which is further simplified for H- and E-plane structures as:

$$S_{ji} = \frac{\frac{1}{\sqrt{I_{10}^{p_j}}} \int_{\Gamma_{p_j}} \mathbf{H}_\Omega(\xi) \cdot \sin \frac{\pi\xi}{a^{p_j}} \mathrm{d}\boldsymbol{\Gamma}_{p_j}}{H_0^{\text{in}} \frac{a^{p_i}}{2} \frac{1}{\sqrt{I_{10}^{p_i}}}} \quad (H\text{-plane}), \tag{34}$$

$$S_{ji} = \frac{\frac{1}{\sqrt{I_{10}^{p_j}}} \int_{\Gamma_{p_j}} \mathbf{E}_\Omega(\eta) \cdot \mathrm{d}\boldsymbol{\Gamma}_{p_j}}{E_0^{\text{in}} b^{p_i} \frac{1}{\sqrt{I_{10}^{p_i}}}} \quad (E\text{- plane}). \tag{35}$$

Specifically, for the E-plane case (35) may be further simplified as follows

$$S_{ji} = \frac{\int_{\Gamma_{p_j}} \mathbf{E}_\Omega(\eta) \cdot \mathrm{d}\boldsymbol{\Gamma}_{p_j}}{E_0^{\text{in}} b^{p_i}} \quad (\text{homogeneous structure}) \tag{36}$$

for homogeneous structures which are the ones that are suitable for the formulation of Section 2.2.2.

3. *hp* Finite elements and automatic adaptivity

In order to solve the presented electromagnetic problems, a numerical technique that provides low discretization errors and, simultaneously, solves the discretized problem without prohibitive computational cost, is needed. In this context, an adaptive *hp*-Finite Element Method satisfies both properties.

3.1. hp Finite elements (FE)

Each finite element is characterized by its size h and order of approximation p. In the h-adaptive version of FE method, element size h may vary from element to element, while order of approximation p is fixed (usually $p = 1, 2$). In the p-adaptive version of the FE method, p may vary locally, while h remains constant throughout the adaptive procedure. Finally, a true *hp*-adaptive version of FE method allows for varying both h and p locally.

The *hp*-FE method used in this paper utilizes edge (Nédélec) elements of variable order of approximation. FE spaces associated to those elements have been carefully constructed (see [25] for details) so in combination with the projection based interpolation operators (defined below), the commutativity of the *de Rham* diagram is guaranteed. This commutativity property is essential for showing convergence and stability of the FE method for electromagnetics [25].

The main motivation for the use of *hp*-FEM is given by the following result: "an optimal sequence of *hp*-grids can achieve exponential convergence for elliptic problems with
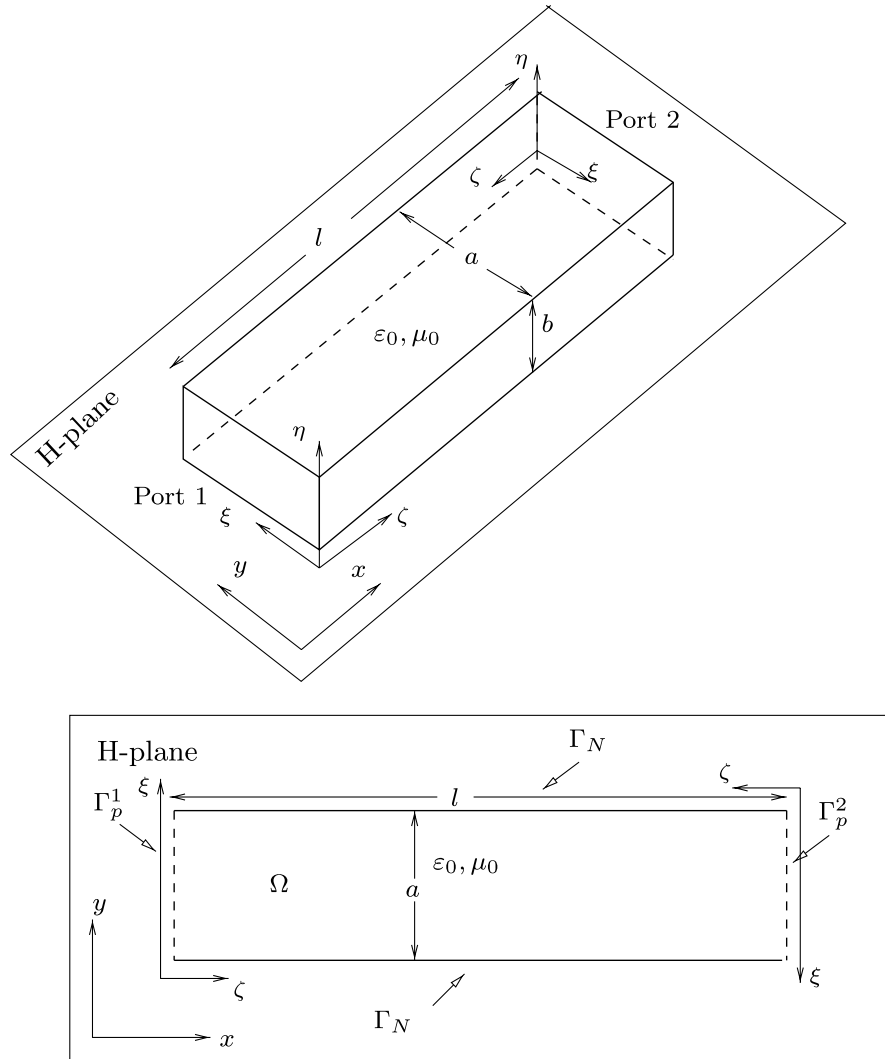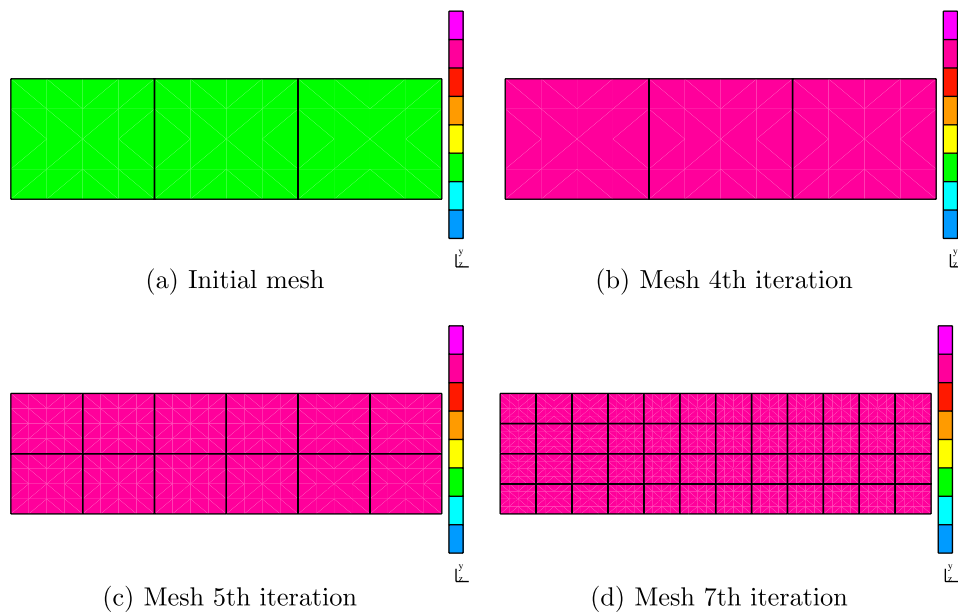
Fig. 7. *H*-plane waveguide section.

(a) Initial mesh

(b) Mesh 4th iteration

(c) Mesh 5th iteration

(d) Mesh 7th iteration

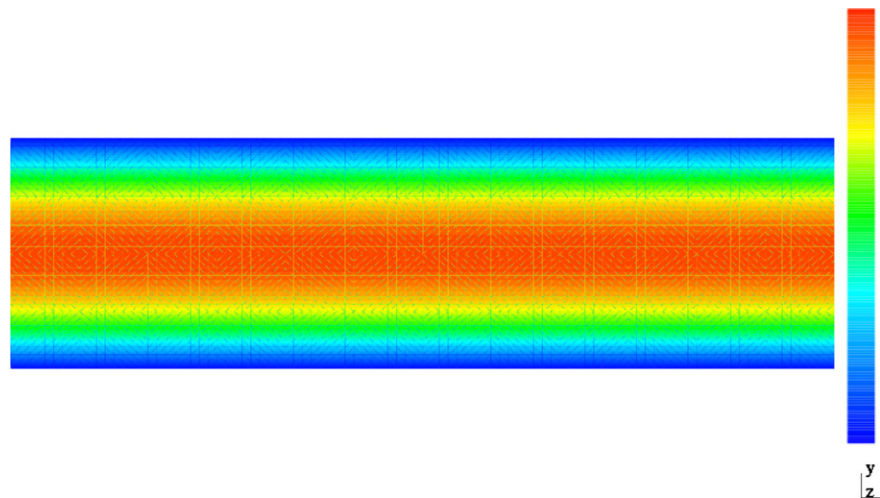Fig. 8. Initial mesh and some *hp* meshes for the *H*-plane waveguide section.

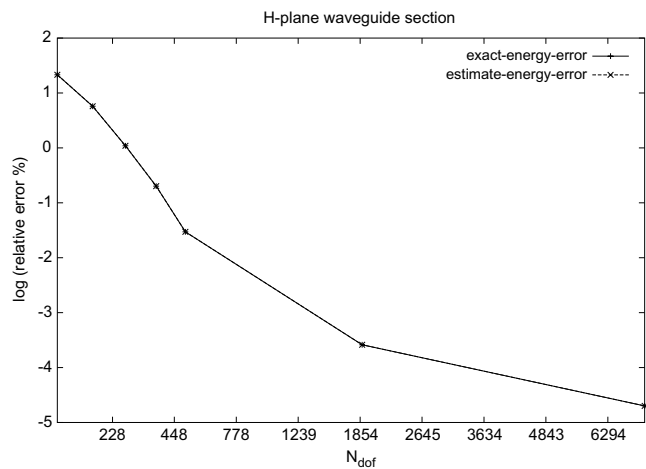Fig. 9. Magnitude of H_y, i.e., $|H_y|$, corresponding to the H-plane waveguide section.

Fig. 10. Convergence history for the H-plane waveguide section (energy norm error for the magnetic field solution).

Table 2
Scattering parameters for the H-plane waveguide section

	$|S_{11}|$	$|S_{21}|$	$\arg(S_{21})$
Iteration 1	1.0302e−02	0.9991183	10.1204°
Iteration 2	5.9652e−04	0.9994050	0.9797°
Iteration 3	4.6872e−07	0.9999995	0.0402°
Iteration 4	2.7117e−07	0.9999997	0.0013°
Analytic	0.0	1.0	0.0°

a piecewise analytic solution, whereas *h*- or *p*-FEM converge at best algebraically'' (see [29–35]).

Next, the fully automatic *hp*-adaptive strategy is presented. Given a problem and a discretization tolerance error, the objective is to generate automatically (without any user interaction) an *hp*-grid that does not exceed the discretization error tolerance and, at the same time, it employs a minimum number of degrees of freedom (d.o.f.), by orchestrating an optimal distribution of element size *h* and polynomial order of approximation *p*. By doing so, it is possible to achieve exponential convergence rates in terms of the error vs. the number of d.o.f.

3.2. Fully automatic hp-adaptivity

The self-adaptive strategy iterates along the following steps. First, a given (coarse) *hp*-mesh is globally refined both in *h* and *p* to yield a *fine mesh*, i.e., each element is broken into four element sons (eight in 3D), and the order

of approximation is raised uniformly by one. Then, the problem of interest is solved on the fine mesh. The difference between the fine and coarse grid solutions is used to guide optimal refinements over the coarse grid. More precisely, the next optimal coarse mesh is then determined by minimizing the *projection based interpolation error* of the fine mesh solution with respect to the optimally refined coarse mesh (see [3,36] for details).

The adaptive strategy is very general, and it applies to H^1-, **H**(curl)-, and **H**(div)-conforming discretizations. Moreover, since the mesh optimization process is based on minimizing the interpolation error rather than the residual, the algorithm is problem independent and it can also be applied to nonlinear and eigenvalue problems.

The *hp* self-adaptive strategy incorporates also a two-grid iterative solver, which allows to solve the fine grid problems efficiently. Indeed, it has been shown in [37,38] that it is sufficient a partially converged fine grid solution to guide optimal *hp*-refinements. Thus, only few two-grid solver iterations are needed (below ten per grid).

In the remainder of this section, the projection based interpolation operator [39,40], which is the main ingredient of the mesh optimization algorithm, is presented first. Then, the mesh optimization algorithm is briefly described.

3.2.1. The projection based interpolation operator

The idea of projection based interpolation operator is based on three properties.
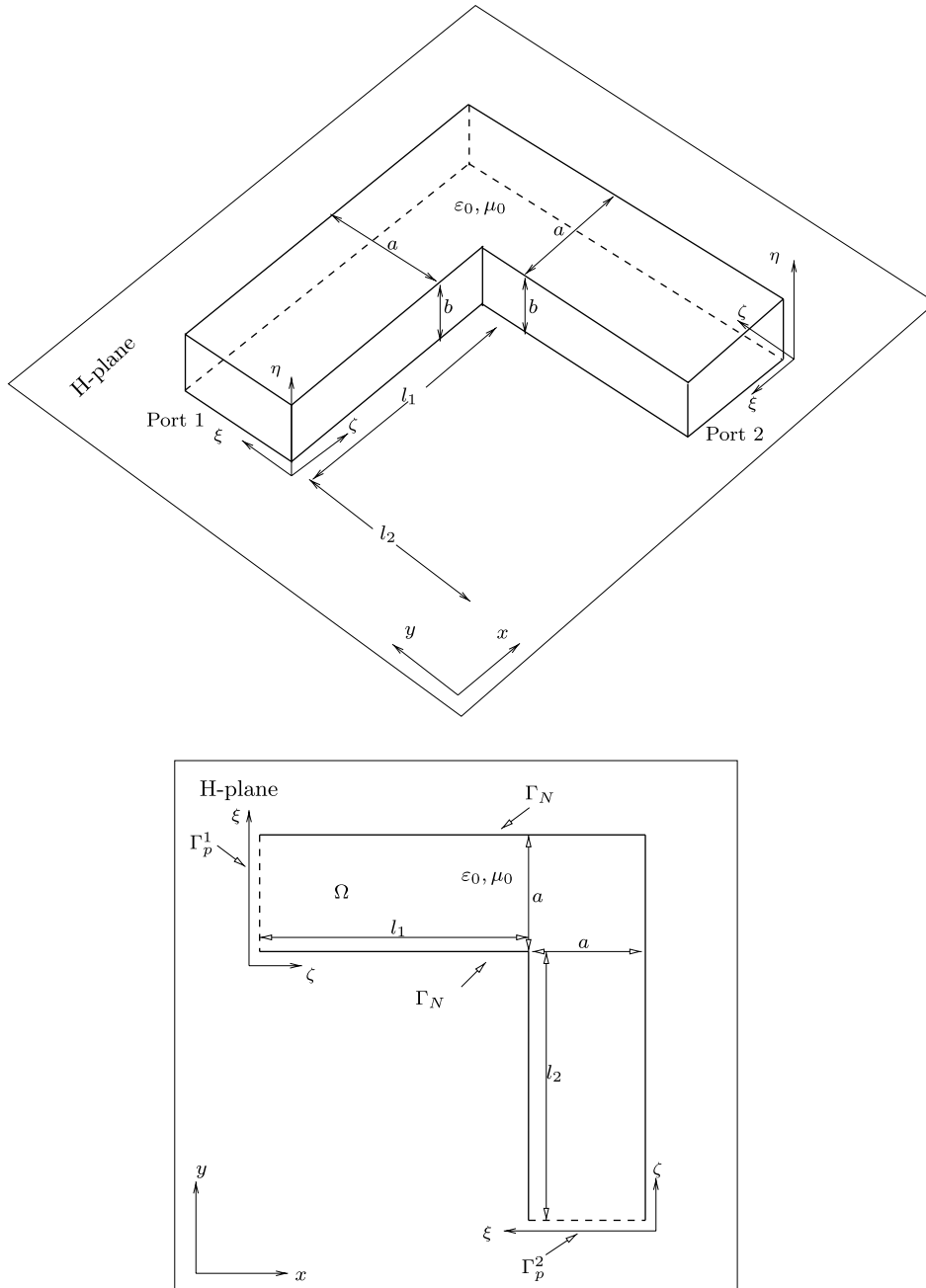
Fig. 11. *H*-plane 90° bend.

- Locality: Determination of element interpolant of a function should involve the values (and derivatives) of the interpolated function in the element only.
- Conformity: The union of element interpolants should be globally conforming.
- Optimality: The interpolation error should behave asymptotically, both in *h* and *p*, in the same way as the actual approximation error.

The H^1-conforming projection based interpolation operator is presented first. Let $u \in H^{1+\epsilon}(K)$ with $\epsilon > 0$. Locality and conformity imply that the interpolant $w = \Pi u$ should match the interpolated function u at vertexes:

$$w|_{\text{vert}} = u|_{\text{vert}}. \tag{37}$$

With the vertex values fixed, we project over each edge, i.e.:

$$w := \arg \min_{v:(v-u)|_{\text{vert}}=0} \|v - u\|_{\text{edge}}. \tag{38}$$

This definition preserves locality and conformity. It also preserves optimality provided that the optimal edge norm is selected, which is dictated by the problem being solved and the Trace Theorem (see [25] for details). For example, in 1D, the optimal edge norm is the H_0^1-norm. In 2D, the $H^{1/2}$-seminorm, and in 3D, the L^2-norm, should be used.

Using the same argument, once vertex and edge values are fixed, projection over the interior of the element (faces
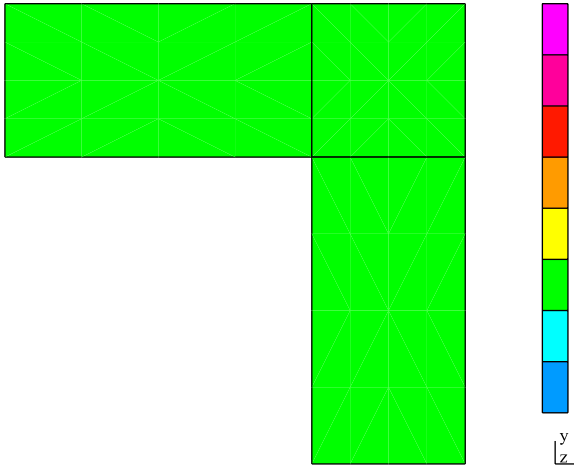
Fig. 12. Initial mesh for the *H*-plane 90° bend.
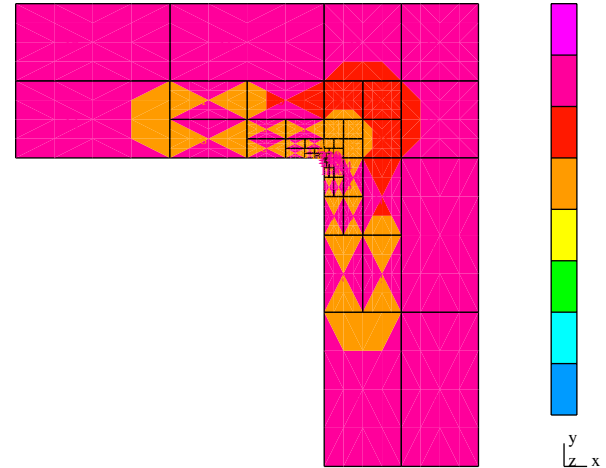
Fig. 14. Final *hp* mesh for the *H*-plane 90° bend.
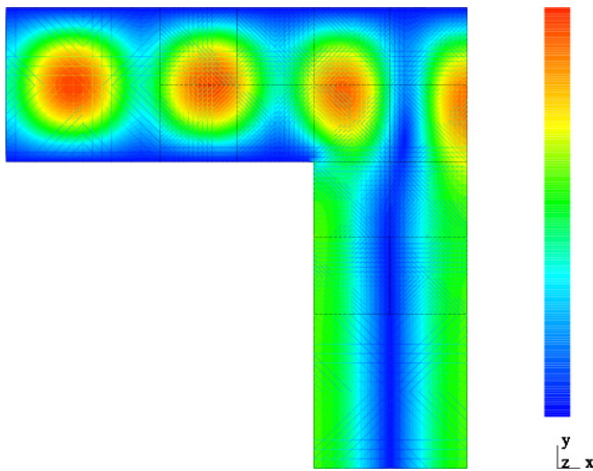
Fig. 13. Magnitude of H_y, i.e., $|H_y|$, corresponding to the *H*-plane 90° bend.
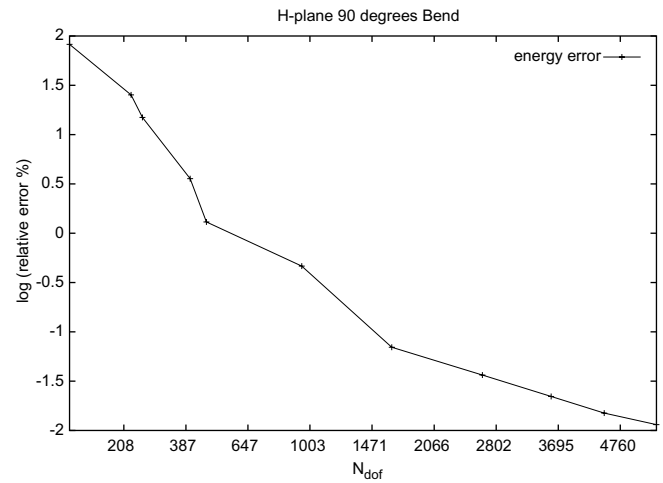
Fig. 15. Convergence history for the *H*-plane 90° bend.

Table 3
Scattering parameters for the *H*-plane 90° bend

	$|S_{11}|$	$|S_{21}|$	$\arg(S_{11})$	$\arg(S_{21})$
Iteration 1	0.5465	0.8372	10.049°	112.615°
Iteration 2	0.4459	0.8951	16.948°	101.604°
Iteration 3	0.4148	0.9099	5.639°	95.665°
Iteration 4	0.4156	0.9096	5.619°	95.617°
MM	0.4161	0.9093	5.345°	95.345°

in 3D) is performed. Thus, the projection based interpolation operator for 2D H^1-problems is formally defined as:

$$w(v) := u(v) \quad \text{for each vertex } v,$$
$$|w - u|_{\frac{1}{2},e} \to \min \quad \text{for each edge } e, \quad (39)$$
$$|w - u|_{1,K} \to \min \quad \text{in the interior of element } K.$$

For a definition of projection based interpolation operator for 3D H^1-problems, see [41].

Similarly, a projection based interpolation operator can be defined for elements in **H**(curl), which is the space of interest for the electromagnetic field. Given $\mathbf{E}$[9] in **H**(curl), the projection based interpolator $\mathbf{\Pi}^{\text{curl}}$ specialized to the 2D case (for the 3D see [39,42]), is denoted by $\mathbf{E}^p = \mathbf{\Pi}^{\text{curl}}\mathbf{E}$, where $\mathbf{E}^p$ is given by:

$$\|\mathbf{E}_t^p - \mathbf{E}_t\|_{-\frac{1}{2},e} \to \min \quad \text{for each edge } e,$$
$$|\nabla \times \mathbf{E}^p - \nabla \times \mathbf{E}|_{0,K} \to \min,$$
$$(\mathbf{E}^p - \mathbf{E}, \nabla\phi)_{0,K} = 0, \quad \text{for every ``bubble'' function,}$$
$$\text{in the interior of element } K.$$

$$(40)$$

Here, the bubble functions come from an appropriate polynomial space mapped by the gradient operator onto the subspace of fields **E** with zero curl and tangential trace on the element boundary.

---

[9] **E** is used here to abstractly denote an element in **H**(curl). In this paper, discretizations in **H**(curl) are used for the magnetic field on the *H*-plane and the electric field on the *E*-plane of the structures.
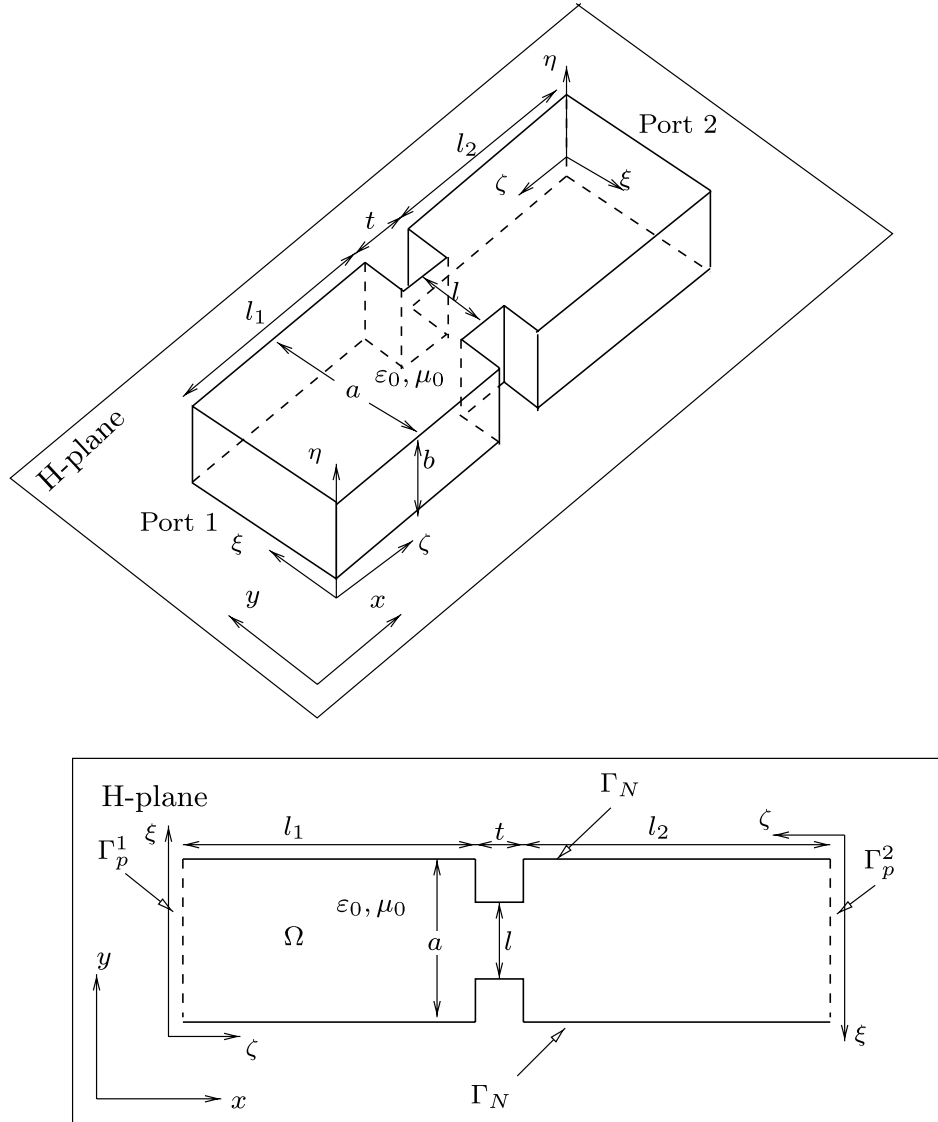
Fig. 16. *H*-plane symmetric inductive iris ($l/a = 0.6$, $t/a = 0.2$).

A similar operator can be defined for $\mathbf{H}(\mathrm{div})$ problems (see [25]).

Finally, it is important to mention that the *de Rham* diagram equipped with these projection based interpolation operators commutes (see [25,11,39] for details), which is critical for proving stability and convergence properties of the FEM for Maxwell equations.

3.2.2. The mesh optimization algorithm

The mesh optimization algorithm in 2D follows the next steps.

- Step 0: Compute an estimate of the approximation error on the coarse grid.

  The approximation error on the coarse grid is estimated by simply computing the norm of the difference between the coarse and the fine grid solutions. If the difference (relative to the fine grid solution norm) is smaller than a requested error tolerance, then the fine mesh solution is delivered as the final solution, and the optimization algorithm finishes.

- Step 1: For each edge in the coarse grid, compute the error decrease rate for the p refinement, and all possible h-refinements.

  Let p_1, p_2 be the order of the edge sons in the case of h-refinement, and let $\mathbf{E} = \mathbf{E}_{h/2,p+1}$ denote the fine grid solution. Then, the error decrease rate is computed as:

$$\text{Error decrease } (\widehat{hp}) = \frac{\|\mathbf{E}_{h/2,p+1} - \mathbf{\Pi}^{\mathrm{curl}}_{hp}\mathbf{E}\| - \|\mathbf{E}_{h/2,p+1} - \mathbf{\Pi}^{\mathrm{curl}}_{\widehat{hp}}\mathbf{E}\|}{(p_1 + p_2 - p)},$$

where $\widehat{hp} = (\hat{h}, \hat{p})$ is such that $\hat{h} \in \{h, h/2\}$. If $\hat{h} = h$, then $\hat{p} = p + 1$. If $\hat{h} = h/2$, then $\hat{p} = (p_1, p_2)$, where $p_1 + p_2 - p > 0$, $\max\{p_1, p_2\} \leqslant p + 1$.
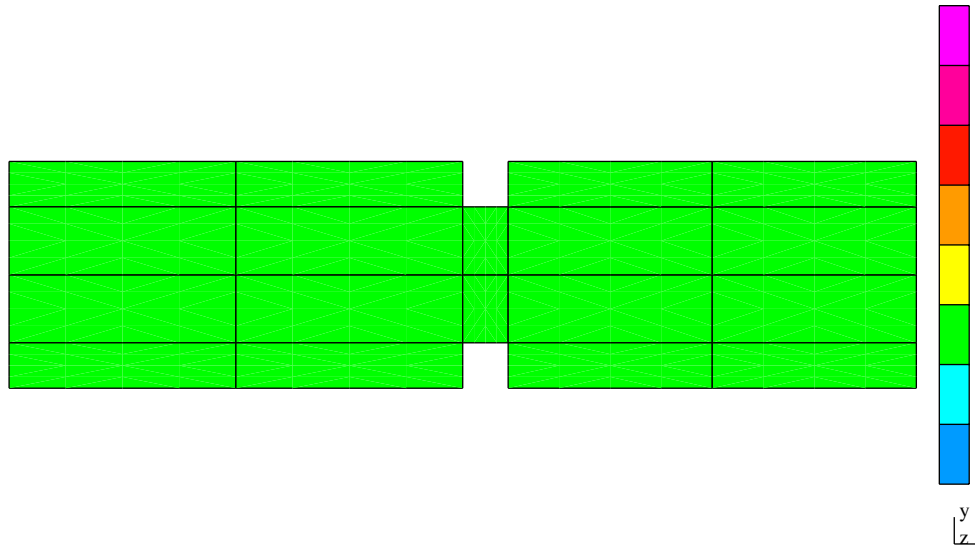
Fig. 17. Initial mesh for the *H*-plane symmetric inductive iris.

- Step 2: For each edge in the coarse mesh, choose between *p* and *h* refinement, and determine the *guaranteed* edge error decrease rate.

  The optimal refinement is found by comparing the error decrease corresponding to the *p*-refinement with all *competitive h*-refinements. Competitive *h*-refinements are those that result in the same increase in the number of degrees-of-freedom (d.o.f.) as the *p*-refinement, i.e., $\hat{h} = h/2$ and $p_1 + p_2 - p = 1$.

  Next, the *guaranteed rate* with which the interpolation error must decrease over the edge is determined. That is, for each edge, the maximum of the error decrease rates for the *p*-refined edge and all possible *h*-refined edges is computed.

- Step 3: Select edges to be refined.

  Given the guaranteed rate for each edge in the mesh, the maximum rate for all elements is calculated

  $$\text{guaranteed rate}_{\max} = \max_e(\text{edge } e \text{ guaranteed rate}).$$

  All edges that produce a rate within 1/3 of the maximum guaranteed rate, are selected for a refinement. The factor 1/3 is somehow arbitrary.

- Step 4: Perform the requested *h*-refinements enforcing the 1-irregularity rule of the mesh.

  A loop through elements of the coarse grid is performed. If at least one edge of the element is to be broken, the element is refined accordingly. As in [3,36], element isotropy flags are computed. Isotropic *h*-refinements are enforced if the error function within the element changes comparably in both element directions.

  After this step, the topology of the new coarse mesh has been determined, and it remains only to establish the optimal distribution of orders of approximation for the *involuntarily h-refined edges*, and for the interior nodes of the element i.e., those nodes that are not located on the boundary of the element. For the interior
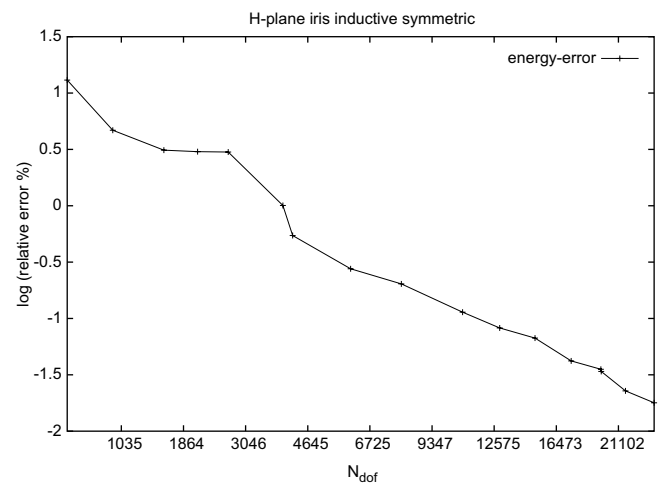
Fig. 18. Convergence history for the *H*-plane inductive iris.

nodes, the starting point for the minimization procedure will be based on the order of approximation *p* for the adjacent edges.[10]

- Step 5: Determine the optimal orders of approximation *p* for the refined edges and elements.

  This step consists basically of *p*-adaptivity over a given grid with the fine grid as a reference solution. Unfortunately, due to the possible presence of involuntary edge *h*-refinements and too low *p* for *h*-refined elements, the interpolation error of the coarse grid after step 4 may actually be larger than the interpolation error for the

---

[10] For triangles, the initial order of approximation will be equal to the maximum of the three edges of the element. For quadrilaterals, we have a horizontal and a vertical order of approximation $p = (p_h, p_v)$. In this case, the starting point for the minimization procedure will be the maximum of the two horizontal edges for p_h and the maximum of the two vertical edges for p_v.
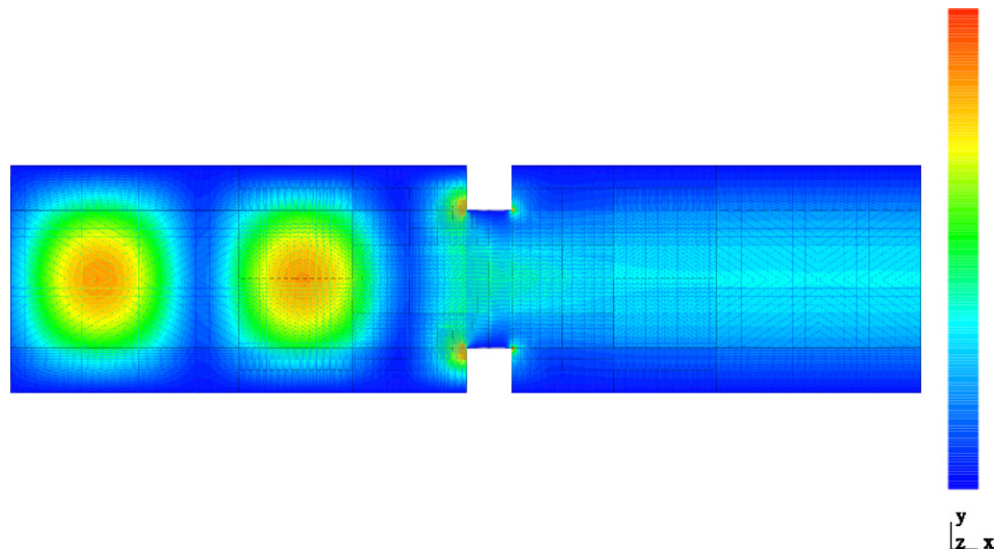
Fig. 19. Magnitude of H_y for the H-plane inductive iris.
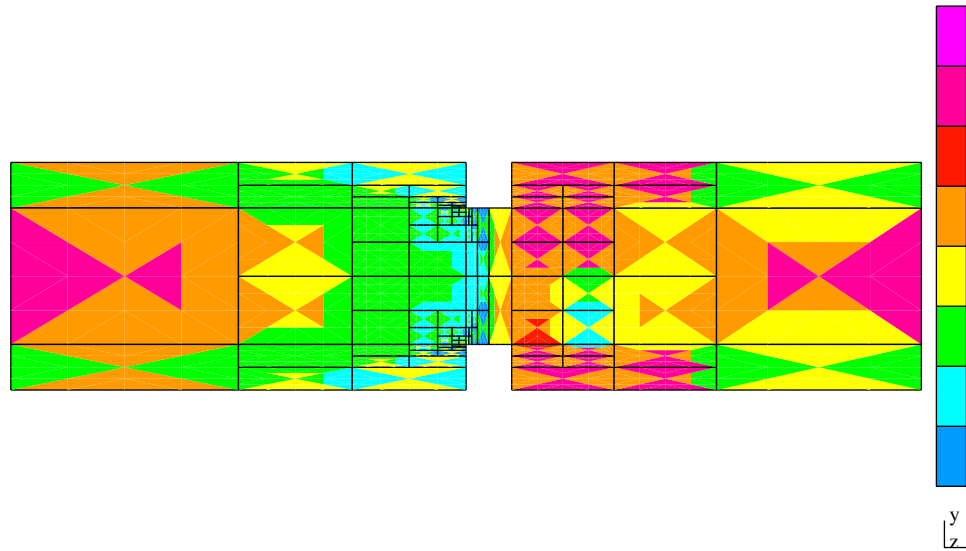
Fig. 20. Eleventh mesh for the H-plane symmetric inductive iris showing heavy h-refinements around the left corners.

original coarse mesh. Thus, extra technical details are considered in order to guarantee interpolation error decrease. These details are quite involving, and are described in [11].

Some remarks on the mesh optimization algorithm follow:

- A similar but yet more involved mesh optimization algorithm has been implemented for 3D problems, although the 3D electromagnetic version is still under development.
- The main difference between the fully automatic hp-adaptive strategy for elliptic and electromagnetic problems resides in the definition of the projection based interpolation operator.

- A similar algorithm can be implemented for $\mathbf{H}(\text{div})$ problems.

4. Numerical results

In the following, a number of rectangular H-plane and E-plane waveguide discontinuities, as well as more complex structures obtained by combining several discontinuities, are analyzed. The analysis of all these structures is performed by using the fully automatic hp-adaptive FE strategy presented above.

TE_{10} mode excitation has been used in all the structures. Also, the ratio of the broad dimension a to the narrow dimension b of the rectangular waveguide sections is considered to be $a/b = 2$. The results correspond to a given
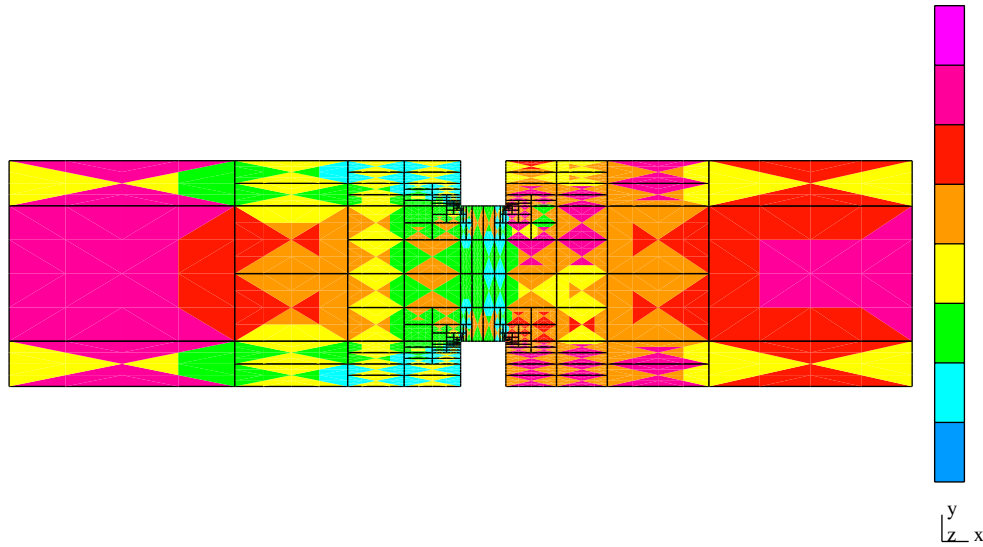
Fig. 21. Nineteenth mesh for the *H*-plane symmetric inductive iris showing heavy *h*-refinements around the left and also right corners.

frequency which is chosen to be in the middle of the mono-mode region, i.e., $k = 1.5k_{c10}$. Exceptionally, the structure analyzed in Section 4.2.3 is solved for a large number of frequencies within a given frequency region, in order to characterize its frequency response. The lengths of the waveguide sections that connect the discontinuity to the ports of the structure are typically around one wavelength for the *H*-plane structures, and around half a wavelength for the *E*-plane structures. This is enough for the first absorbing boundary condition used at the ports to perform correctly. The reason why the length of the waveguide sections is lower for the *E*-plane structures is the following. The same 2D domain (obviously with different b.c.) is used for the same kind of discontinuity, independently of analyzing it with the *H*-plane or *E*-plane formulation. Thus, a given length of a port in the 2D problem domain corresponds to the broad dimension *a* or narrow dimension *b* of the rectangular waveguide at that port, depending on the formulation used. As a consequence, the cut-off frequency is affected and, hence, the propagation constant *β*. Thus, the same physical length of a given waveguide port correspond to different electrical lengths for the *E*-plane and *H*-plane cases; being half the electrical length of the *E*-plane case when compared with the *H*-plane case due to the relation $a/b = 2$ is satisfied.

Typically, quite coarse meshes are used as initial grids in order to assess the robustness of the *hp* strategy in the context of real engineering analysis in which the initial mesh has to be as coarse as possible to simplify the mesh generation process. The convergence history is always shown using a log scale for the energy error (in percent of the energy-norm) in the ordinate axis and a scale corresponding to $N_{dof}^{1/3}$ (being N_{dof} the number of degrees of freedom in the mesh) in the abscissa axis. Thus, according to [34] and references therein, an straight line should appear in the plot showing the theoretical exponential convergence

Table 4
Scattering parameters for the *H*-plane symmetric inductive iris

	$|S_{11}|$	$|S_{21}|$	$\arg(S_{11})$	$\arg(S_{21})$
Iteration 2	0.7333	0.6799	−157.92°	−27.243°
Iteration 4	0.7401	0.6725	−156.59°	−26.325°
Iteration 6	0.7386	0.6741	−156.48°	−26.588°
Iteration 8	0.7414	0.6711	−156.46°	−26.287°
MM	0.7417	0.6708	−156.51°	−26.259°

that can be achieved with an optimal *hp* adaptivity strategy. Note that the abscissas scale corresponds to $N_{dof}^{1/3}$ while abscissas axis tics should be read as N_{dof} in the plots.

The scattering parameters obtained using the *hp*-FEM are compared with values computed with the Mode Matching (MM) method (see e.g., [12], [13, Chapter 9]). The MM method can be considered as a semi-analytic method. It consists of the decomposition of the domain of the problem into several simple domains, typically with translational symmetry, in which, an analytical modal expansion can be performed. Imposing the tangential continuity of the field and orthogonality of the modes yields a system of equations in which the unknowns are the coefficients of the modal expansions.

The FEM scattering parameter results delivered from the *hp* adaptivity are more accurate than MM results. In this context, it is important to point out that MM results are typically considered as a reference for the engineering analysis of discontinuities in rectangular waveguide technology, as for the structures shown below. In addition, the *hp*-FE technology enables modeling of more complex structures which cannot be solved using the MM.

4.1. H-plane discontinuities

The analysis of several *H*-plane discontinuities is considered next. The boundary condition of the metallic conduc-

tors represents a Neumann boundary condition for the *H*-plane formulation.

4.1.1. H-plane waveguide section

The first structure shown in Fig. 7 is a simple rectangular waveguide section. This structure is selected as a first verification of the code, specifically for the boundary conditions at the ports and the control of the dispersion error. Since there is no discontinuity in the translational symmetry for this structure, it may be analyzed by means of either the *H*-plane or *E*-plane formulations. Results shown in this section correspond to the *H*-plane analysis. Also, because there is no discontinuity, the scattering parameters of the structure are known to be $S_{11} = S_{22} = 0$ and $S_{21} = S_{12} = \exp(-j\beta_{10}l)$, where l denotes the waveguide section length. In this case, l is equal to 2 wavelengths and, thus, $S_{21} = S_{12} = \exp(-j4\pi) = 1$. The field solution is also known: it corresponds to the field TE_{10} mode inside of the waveguide section.

The solution is smooth: a half-sine type variation in the y direction (the $\pm\xi$ local axis of the waveguide) and constant in amplitude and phase variation as $\exp(-j\beta_{10}x)$ along the x-direction (the $\pm\zeta$ local axis of the waveguide). Thus, the *hp*-adaptive strategy is expected to deliver an increase in the polynomial order of approximation p. The initial mesh used for the analysis is shown in Fig. 8 together
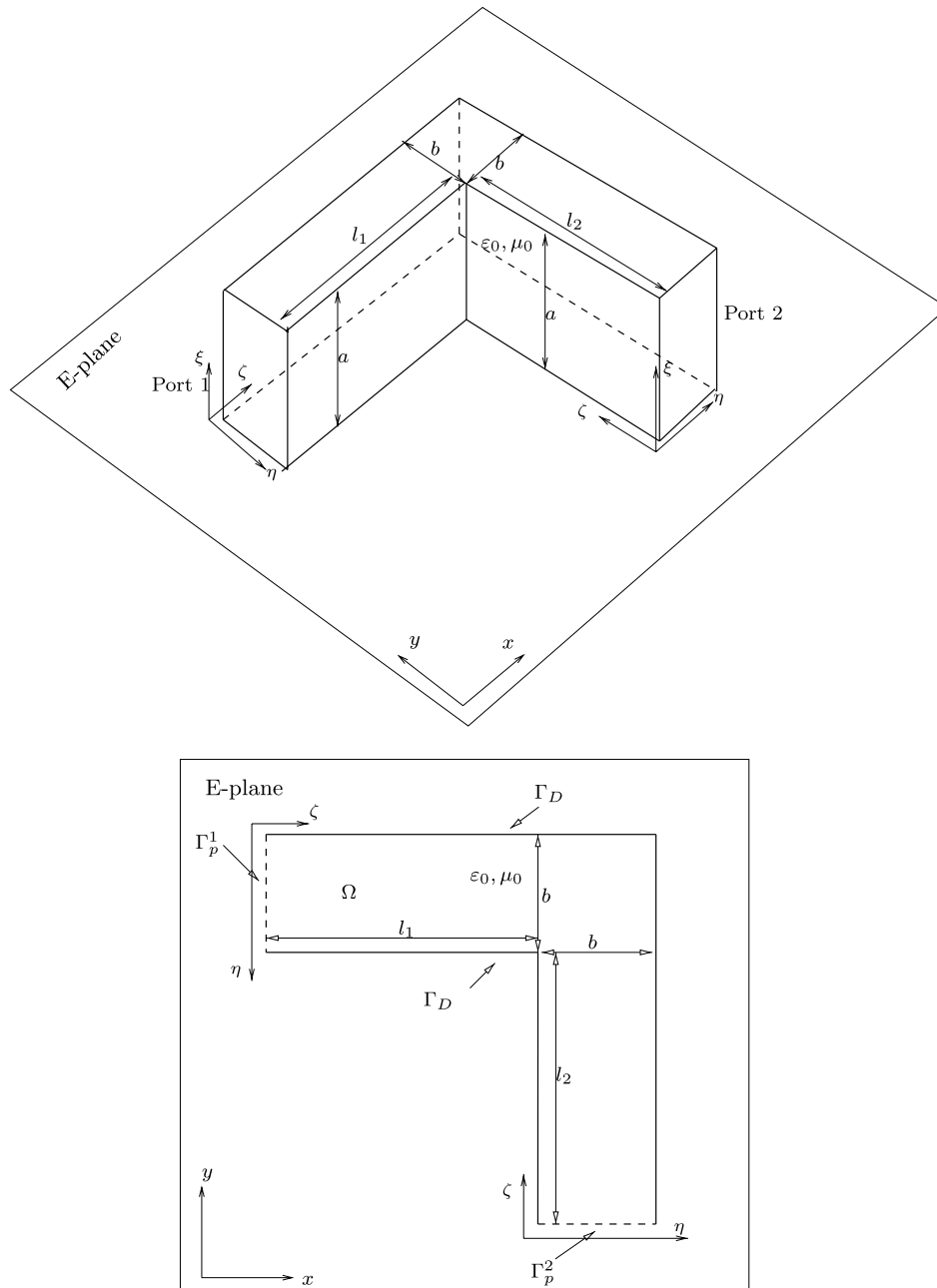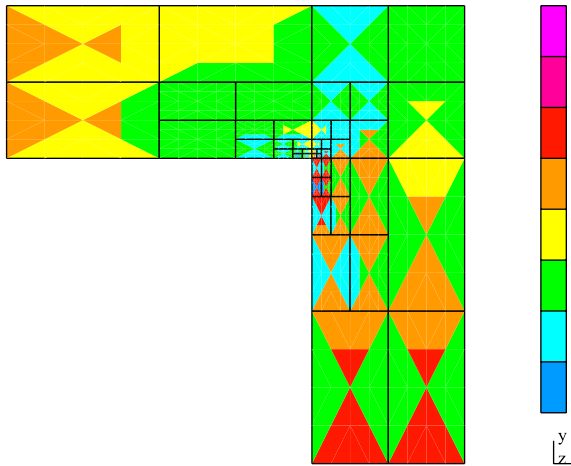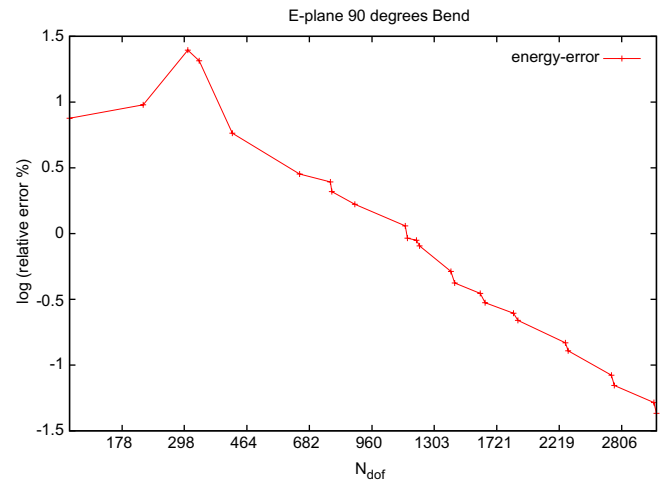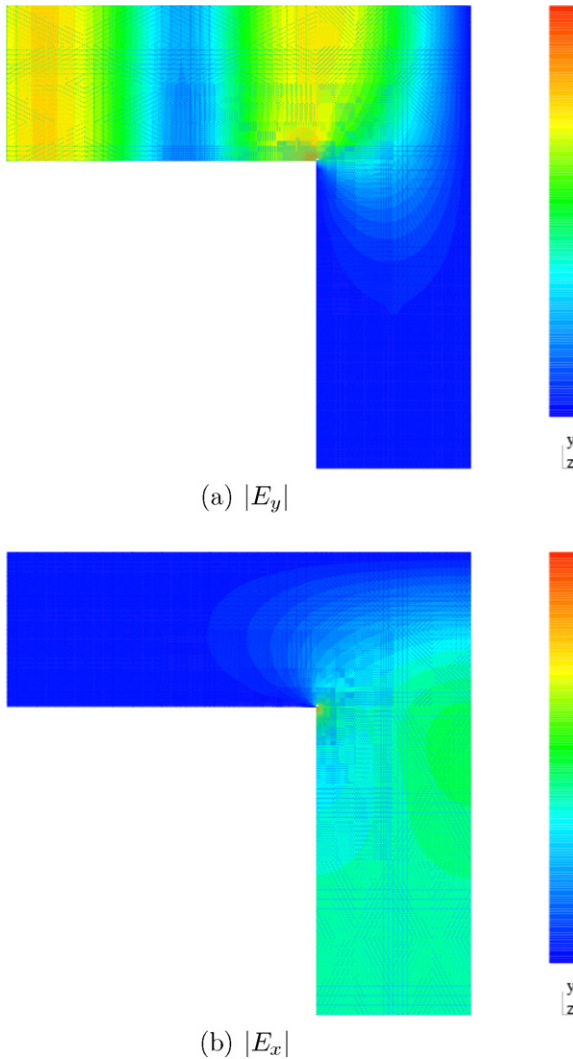

Fig. 22. *E*-plane 90° bend.

Fig. 23. *hp* mesh of 11th iteration of the *E*-plane 90° bend.

(a) $|E_y|$

(b) $|E_x|$

Fig. 24. Magnitudes of E_y and E_x corresponding to the *E*-plane 90° bend showing a singular behavior of the field at the corner.

Fig. 25. Convergence history for the *E*-plane 90° bend.

Table 5
Scattering parameters for the *E*-plane 90° bend

	$|S_{11}|$	$|S_{21}|$	$\arg(S_{11})$	$\arg(S_{21})$
Iteration 1	0.5542	0.8323	−47.810°	−137.81°
Iteration 4	0.5387	0.8425	−46.794°	−136.94°
Iteration 7	0.5487	0.8360	−48.590°	−138.45°
Iteration 10	0.5499	0.8352	−48.558°	−138.49°
MM	0.5507	0.8347	−48.462°	−138.46°

ments. It is important to note that the order corresponds to the H^1 Lagrange multiplier and that the field of **H**(curl) is of order $p - 1$. As an example, the green color of the initial mesh of Fig. 8a indicate that all elements are of order 3 for the Lagrange multiplier and order 2 for the magnetic field. It is observed that order p is increased until the maximum p ($p = 9$) is reached in the fine grid; from this moment, h refinement is selected until the specified error criterion is satisfied.

The convergence history for the exact error and the estimated error is plotted in Fig. 10, showing the quality of the error estimation and the exponential behavior of the error. The exponential convergence is deduced from the observance of a straight line in the plot for the log type ordinates axis and the $N_{dof}^{1/3}$ scale in the abscissas axis set in the figure. It is worth noting that the slope change in the convergence history corresponds to the moment when the maximum p is reached, so h refinements are forced. In other words, this slowdown in convergence would not have occurred if higher order elements were allowed. A plot of the field in the structure, specifically, $|H_y|$, is shown in Fig. 9. In this field plot, as in the other field plots shown in the paper, the colors indicate the intensity of the magnitude of the corresponding field component (H_y in this case) in linear scale, corresponding the blue color to zero value and the orange/red color to the maximum value of the field. It is clearly observed in Fig. 9 the sine and the zero variations along the y and x-axis, respectively. Note that the the zero

with some intermediate meshes. The colors indicate, according to the scale on the right, the order p of the ele-
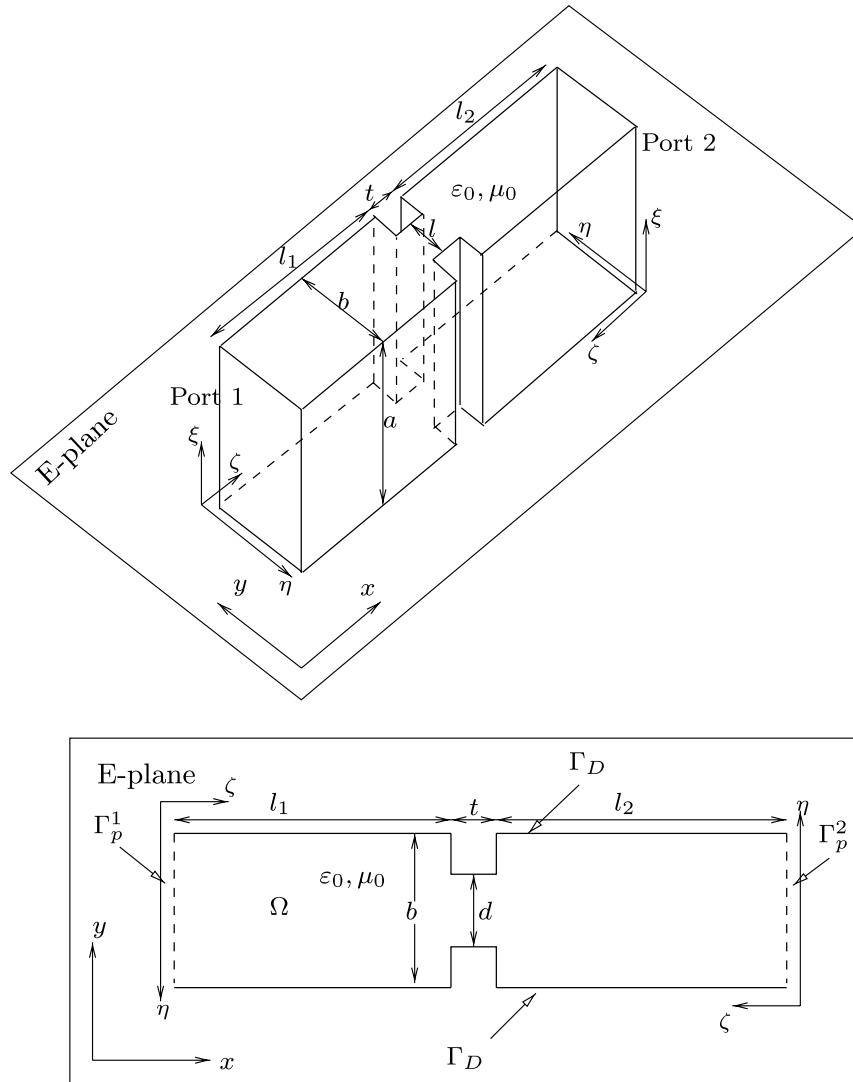
Fig. 26. *E*-plane capacitive symmetric iris ($d/b = 0.6$, $t/b = 0.2$).

variation along the *x*-axis is because we are referring to $|H_y|$ and not H_y. A constant magnitude in the direction of propagation means that there is only one wave in the waveguide and, thus, $|H_y| = |H_0^{\text{in}}||\sin(\pi\zeta/a)|$, so it does not depend on the $\zeta \equiv \pm x$-direction. If a discontinuity had generated a reflected wave, a stationary wave pattern would have been observed at the input waveguide (as it is seen in the examples below).

The scattering parameters have been computed at each iteration step of the *hp* strategy. Due to the reciprocity and symmetry of the structure, the scattering behavior of the discontinuity is characterized by performing one analysis (exciting any of the two ports). The results for the first iterations are shown in Table 2. A fast convergence is observed.

4.1.2. H-plane right angle bend

An *H*-plane 90° bend is analyzed next. The structure is shown in Fig. 11. The structure is analyzed by exciting port

1 (on the left). The bend is a common part of microwave circuits. The initial mesh used for the analysis is shown in Fig. 12. Despite the coarseness of this mesh, the *hp*-strategy achieves an energy error below 1% after 5 iterations. The convergence history (up to an error as low as 0.01%) is shown in Fig. 15. The final mesh is shown in Fig. 14. Heavy *h*-refinements of the mesh around the corner are observed. The *hp*-strategy in this case tends also to increase the *p*. Actually, all elements of the final mesh (except those near the corner) have reached the maximum *p* order. This is the right strategy, since the solution of the problem is smooth (the boundary condition at the conductors for the *H*-plane formulation is of homogeneous Neumann type[11]). The *h*-refinement around the corner is precisely due to the fact that the maximum *p* has been reached

---

[11] The same domain but with Dirichlet boundary conditions corresponds to the *E*-plane bend which is analyzed in Section 4.2.1.
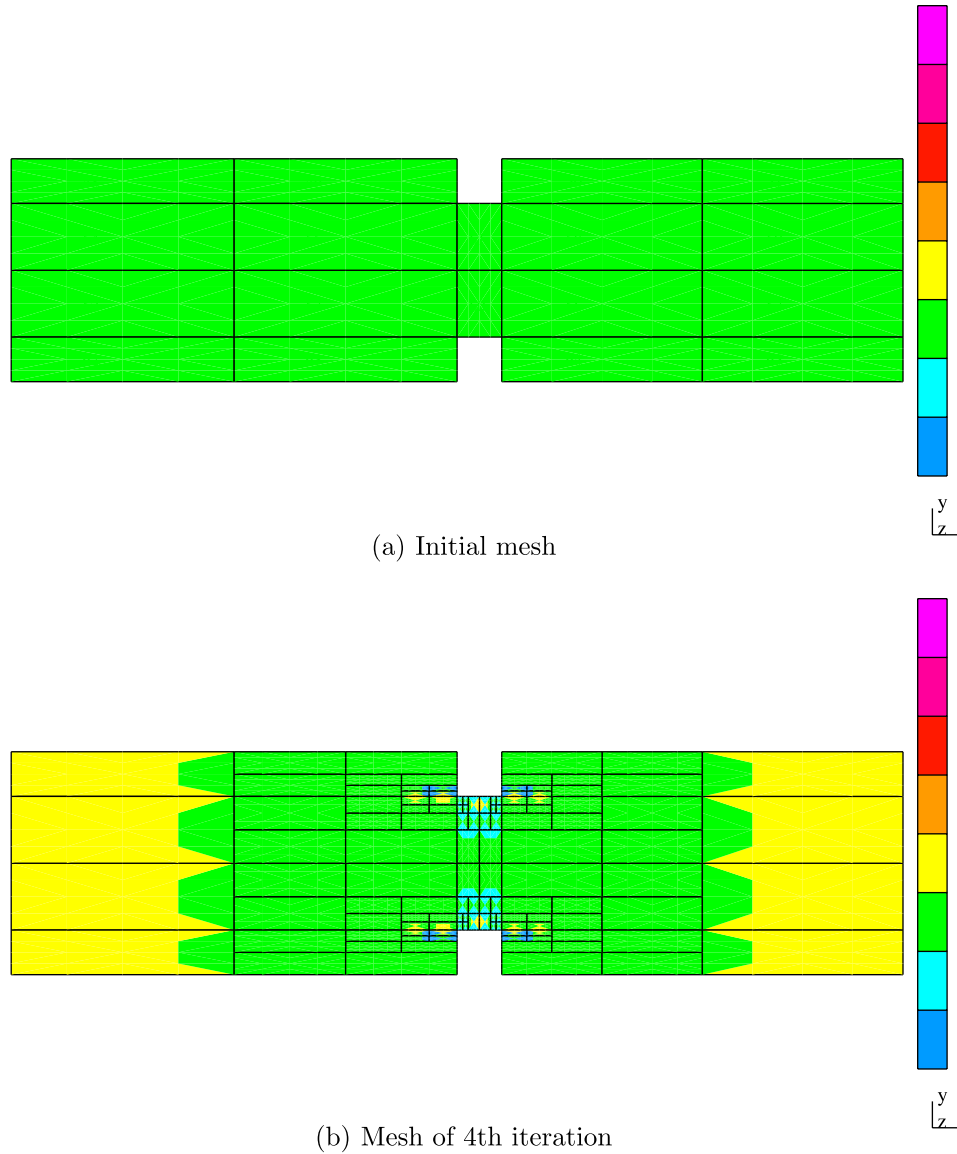
(a) Initial mesh

(b) Mesh of 4th iteration

Fig. 27. Initial mesh and mesh of the fourth iteration for the *E*-plane capacitive symmetric iris.

and, in order to reduce the error in this region, the elements must be made smaller.

A plot of the field in the structure, specifically, $|H_y|$, is shown in Fig. 13. The *y*-component corresponds to the local ξ component at the excitation port and the local ζ component at the transmitted port. Notice in the figure the stationary wave pattern corresponding to the input waveguide (between the excitation port and the bend) because of the combination of the two waves propagating in opposite directions (the excited wave and the reflected wave at the bend). No stationary wave is observed in the output waveguide as there is only one wave propagating outward the transmitted port. As in the previous case, $S_{21} = S_{12}$ and $S_{22} = S_{11}$. The results for S_{11} and S_{21} are shown (for some of the *hp* meshes) in Table 3. The scattering parameters computed with the *hp*-FEM method are compared with those obtained with a MM technique. Only
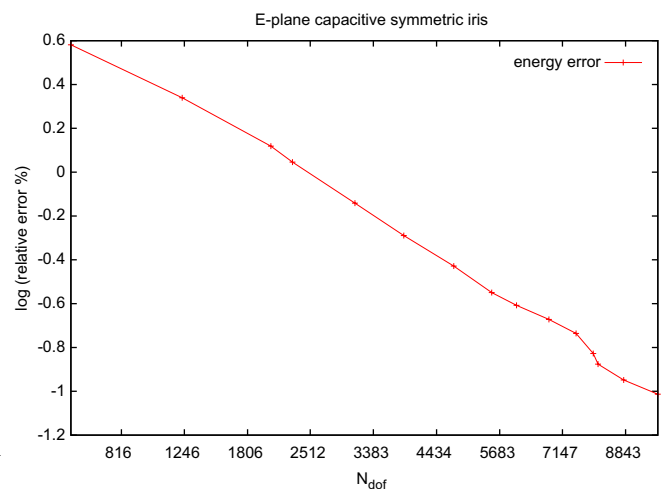

Fig. 28. Convergence history for the *E*-plane capacitive symmetric iris.
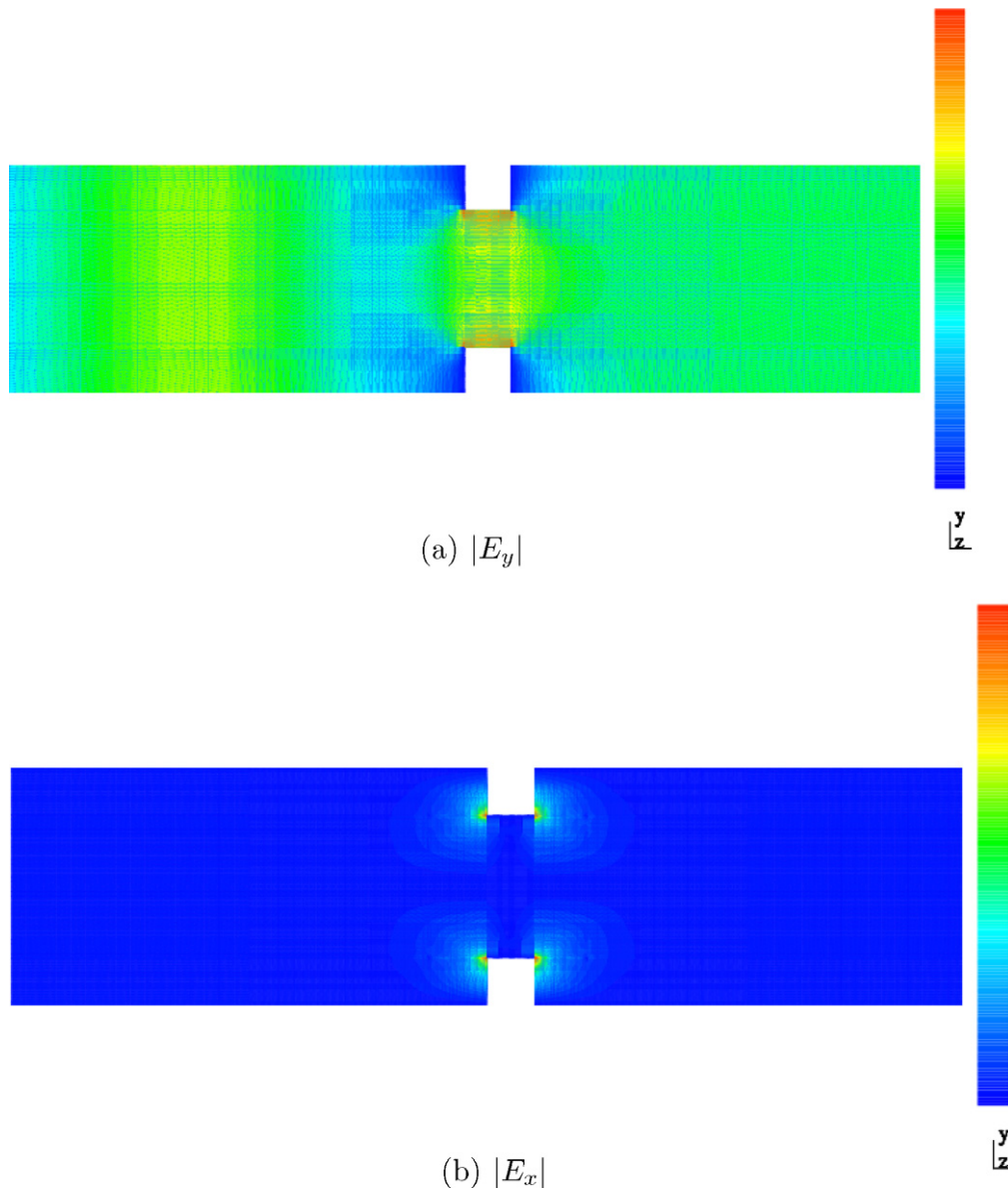
(a) $|E_y|$

(b) $|E_x|$

Fig. 29. Magnitude of E_y and E_x corresponding to the E-plane capacitive symmetric iris.

four significant digits are shown in the table as the MM results are presumed to have no more than four digits of accuracy.[12] Observe the very good agreement of the *hp*-FEM results with those provided by MM; better than 1% after the second iteration. After the fourth/fifth iteration, the FEM results seem to be more accurate than those provided by the MM, as implied by the convergence pattern shown in the table.

4.1.3. H-plane symmetric inductive iris

The next structure is shown in Fig. 16. The discontinuity consists of the narrowing of the broad dimension of the waveguide along a certain length. This region is referred to as an *iris*.[13] Because the iris is centered with respect to the waveguide broad dimension, it is called a *symmetric iris*. Finally, the term inductive is also utilized because the discontinuity scattering behavior with respect to the planes of the discontinuity is equivalent to an inductance. The character of the discontinuity, inductive or capacitive, can be deduced by observing which field lines (electric or magnetic) of the waveguide mode (the TE_{10} in this case) are "cut" by the discontinuity [1]. It is clear from Fig. 16 that only the magnetic field lines are cut in this case (the electric field of the TE_{10} is perpendicular to the *H*-plane of the waveguide). Thus, the symmetric iris of Fig. 16 is

---

[12] This is concluded after making higher the number of modes in the modal expansions and observing fluctuations at the fifth digit level of the values of the S-parameters.

[13] The term *iris* is used in this context to refer to an aperture that connects two waveguide sections.

Table 6
Scattering parameters for the *E*-plane capacitive symmetric iris

	$|S_{11}|$	$|S_{21}|$	$\arg(S_{11})$	$\arg(S_{21})$
Iteration 1	0.3180	0.9481	−163.31°	−53.24°
Iteration 2	0.3070	0.9517	−162.71°	−52.60°
Iteration 5	0.3013	0.9535	−162.37°	−52.25°
Iteration 6	0.3009	0.9537	−162.35°	−52.22°
MM	0.3008	0.9537	−162.36°	−52.23°

of the inductive type. An analogous structure, but of capacitive type, is considered in Section 4.2.2.

The initial mesh used for the analysis is shown in Fig. 17. The analysis is made by exciting port 1 (at the left). The convergence history (up to an error as low as 0.02%) is shown in Fig. 18. Notice the exponential convergence of the method.

A plot of the field in the structure, specifically, $|H_y|$, is shown in Fig. 19. The *y*-component corresponds to the $\pm\xi$ component of the field modes in the waveguide. Observe the stationary wave pattern at the input port due to the wave reflected from the discontinuity and a singular behavior of the field at the re-entrant corners. The magnitude of the fields is higher at the left corners. This is "caught" by the *hp* strategy that refines around the left corners during the first few iterations, and once the error around the left corners is controlled (comparable to other regions of the structure), it starts to "see" the error corresponding to the region around the right corners (see Figs. 20 and 21).
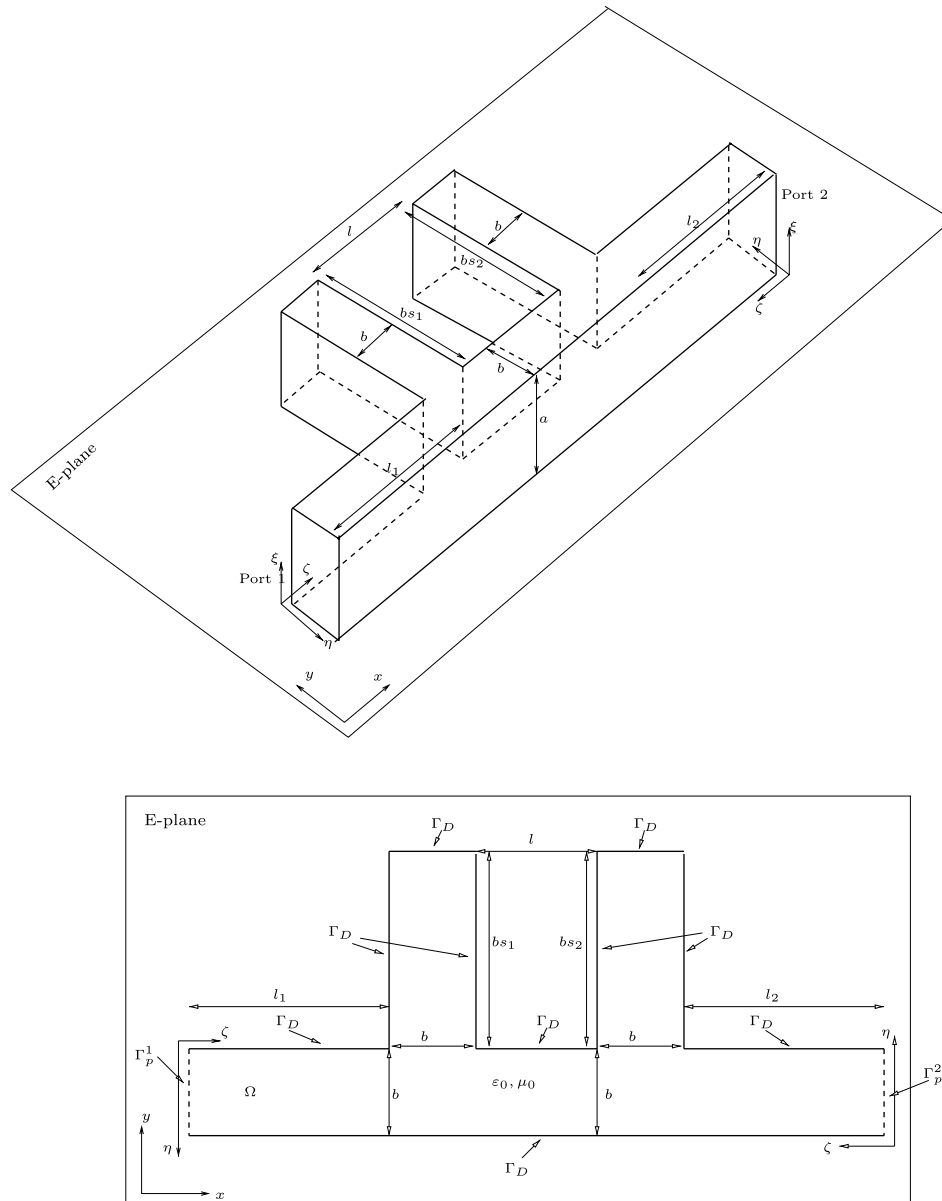

Fig. 30. *E*-plane double stub structure ($bs_1/b = bs_2/b = 5.0249$, $l/b = 1.2608$).
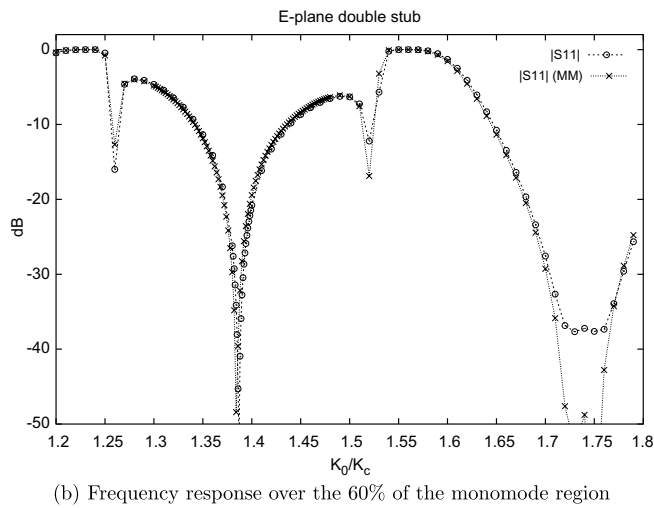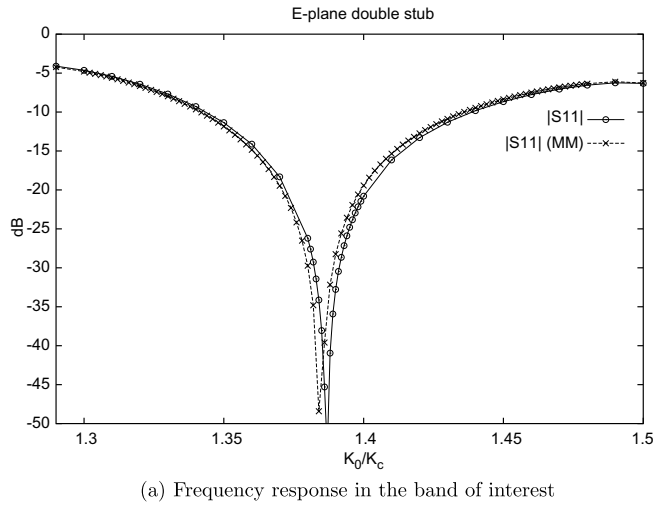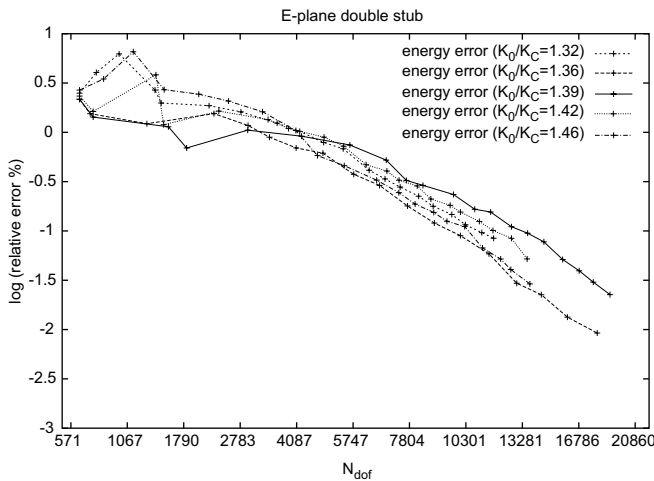
(a) Frequency response in the band of interest

(b) Frequency response over the 60% of the monomode region

Fig. 31. Frequency response of *E*-plane double stub section ($|S_{11}|$ in dB).

Fig. 32. Convergence history for the *E*-plane double stub section.

As in the previous case, $S_{21} = S_{12}$ and $S_{22} = S_{11}$. The results for S_{11} and S_{21} are shown (for some of the *hp*

meshes) in Table 4. Only the results of the first iterations are shown as the *hp* FEM results for the consecutive meshes are, again, presumed to be more accurate than those of MM. Observations analogous to those mentioned in the previous case may be made here.

4.2. E-plane discontinuities

The analysis of several *E*-plane discontinuities is considered next. In contrast to the *H*-plane formulation, the boundary condition of the metallic conductors is of the Dirichlet type for the *E*-plane formulation.

4.2.1. E-plane right angle bend

This discontinuity (Fig. 22) is as the one of Section 4.1.2, a 90 degrees bend. However, the plane of the bend in this case is the *E*-plane. The domain shape is the same as for the *H*-plane bend (actually, the initial mesh is also the same, see Fig. 12) but, this time, the homogeneous Dirichlet boundary condition at the conductors are employed. This, apparently, produces a field singularity that occurs at the corner. The *hp*-strategy behaves as expected and, in contrast to the *H*-plane bend case, an *h*-refinement toward the singularity is observed while increasing the *p* backward. One of the meshes obtained by the *hp*-adaptivity procedure is shown in Fig. 23.

Plots of the field component magnitudes $|E_y|$ and $|E_x|$ are shown in Fig. 24. A stationary wave pattern is observed in the input waveguide (between the excitation port and the bend). The *y*-component corresponds to the component along the local $-\eta$ axis of the excitation port and the component along the ζ local axis of the transmitted port. Since the TE_{10} does not have ζ component, the E_y component is null (numerically null provided that the port is far enough from the discontinuity) at the transmitted port (port 2). Analogously, the E_x component is null at the incident port.

The convergence history is shown in Fig. 25. Except for the peak around the third *hp* iteration (due to the coarseness of the initial mesh), the error shows an exponential decay. With respect to the convergence of the scattering parameters, Table 5 shows their values (in magnitude and phase) for some of the iterations. The MM results are shown for comparison purposes. A good agreement is observed. It is worth noting again that only the results up to the 10th iteration are shown, since the error in the scattering parameters obtained from the *hp* meshes (for iterations higher than the 10th) is lower than the one coming from the MM results.

4.2.2. E-plane capacitive symmetric iris

This discontinuity (Fig. 26) is due to a symmetric iris (as the one of Section 4.1.3), but in the *E*-plane. Thus, the FEM domain is identical to the one used for the *H*-plane inductive symmetric iris, but with different boundary conditions on the conductors boundaries (of Dirichlet type for
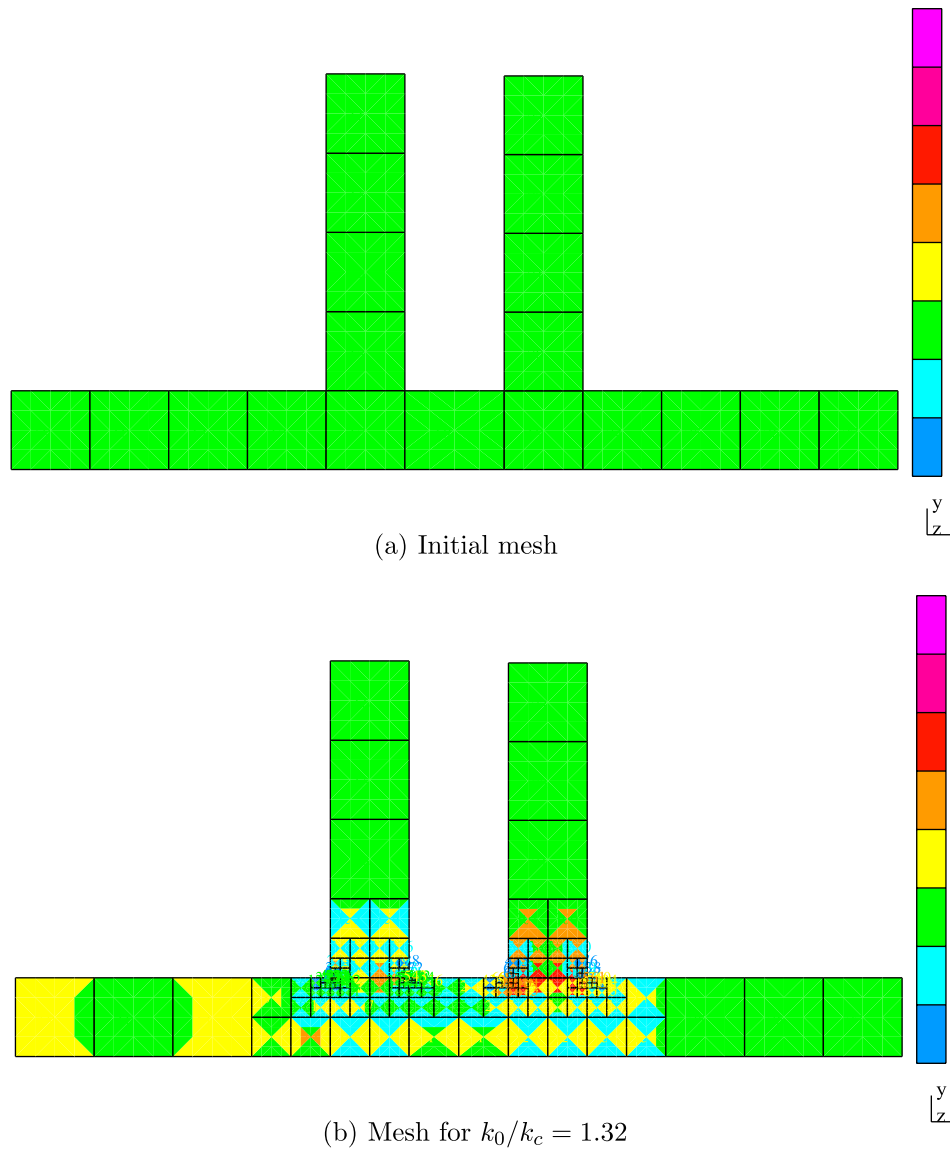
(a) Initial mesh

(b) Mesh for $k_0/k_c = 1.32$

Fig. 33. Initial mesh and mesh corresponding to 1% energy error for the *E*-plane double stub section.

this case). The analysis is made by exciting port 1 (on the left).

The initial mesh is shown in Fig. 27a. Fig. 27b shows a sample mesh corresponding to the fourth iteration. A refinement pattern around the corners of the iris is observed due to the presence of field singularities at those locations. The convergence history (up to an error as low as 0.1%) is shown in Fig. 28. Exponential convergence is again observed.

Plots of the field component magnitudes $|E_y|$ and $|E_x|$ are shown in Fig. 29. A stationary wave pattern is observed in the input waveguide (between the excitation port and the iris) as well as a singular behavior of the field at the corners of the iris. The *y*-component of the field in the structure corresponds to the $\mp\eta$ component of the waveguide modes. Analogously, the *x*-component corresponds to the $\pm\zeta$ component of the waveguide. Thus, the E_x component of the field is generated at the discontinuity, and it is only significant close to it.

The results for S_{11} and S_{21} corresponding to some of the iterations of the *hp* adaptivity are shown in Table 6. The equalities $S_{21} = S_{12}$ and $S_{22} = S_{11}$ hold due to reciprocity and symmetry of the structure. Only the results of the first iterations are shown as the *hp* FEM results for the consecutive meshes are presumed to be more accurate than those of MM.

4.2.3. E-plane double stub section

The structure is shown in Fig. 30. It consists of a main waveguide going from port 1 to port 2 and two waveguides loading it (referred to as *stubs*). The stubs are closed at their ends causing a total reflection of the energy at their inputs. Thus, the load impedance that they present to the main waveguide is purely imaginary. The behavior of this structure may be roughly explained as follows. The load of each stub is like a discontinuity in the waveguide, producing a reflected wave (and also a transmitted wave) with
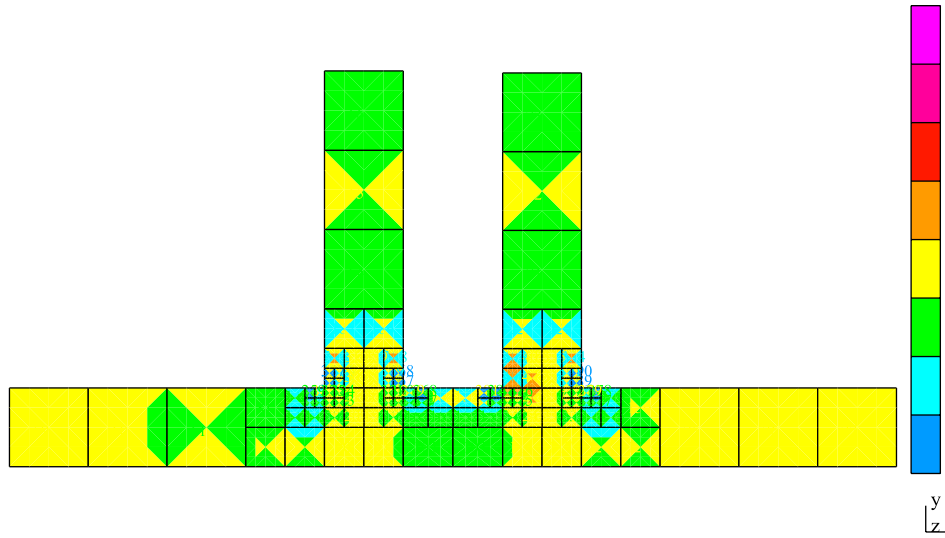
(a) Mesh for $k_0/k_c = 1.36$
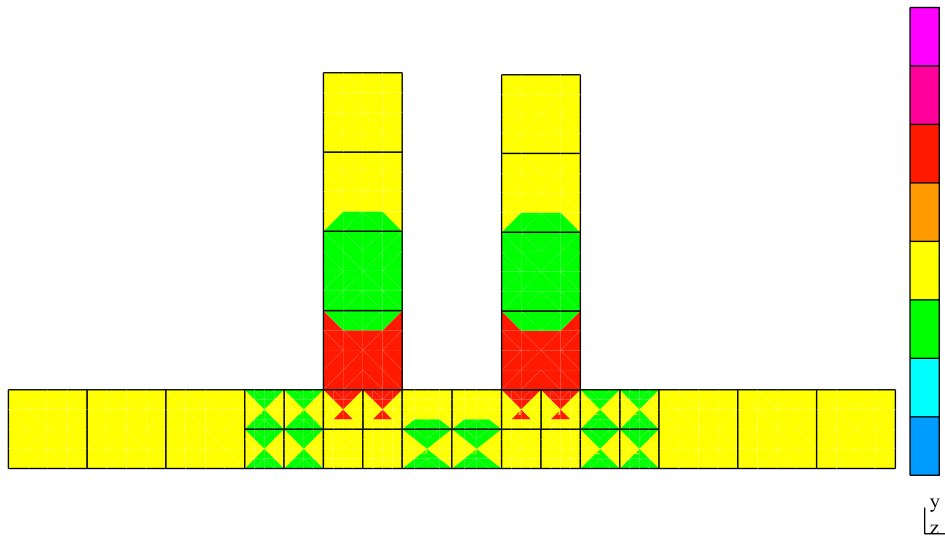
(b) Mesh for $k_0/k_c = 1.39$

Fig. 34. Meshes corresponding to 1% energy error for the *E*-plane double stub section.

a given phase. As there are two stubs, i.e., two discontinuities, the contributions from the two stubs may (totally or partially) add or cancel, depending on the relative phase between the corresponding waves. The relative phase depends (for given stubs dimensions) on the electrical distance θ_d between them. As the electrical distance depends on the frequency for a given physical distance d, i.e., $\theta_d = \beta_{10}d$, the frequency response can be adjusted for several applications. For example, the double stub section can be designed to work as a phase shifter, i.e., causing an extra shift in the phase of the wave at the transmitted port for a given frequency band. This is done by designing the double stub in such a way that there is an adding interference at the transmitted port of the two waves generated by the stubs (with a given phase). Another usual application is an impedance matching network, i.e., the double stub is designed to compensate the reflection present at a given port, due to, e.g., a change in the height of the waveguide, in a given frequency band. This is done by adjusting the design so there is a cancellation of the two reflected waves at the stubs junctions (180° out of phase with respect to each other).

Here, the double stub has been designed for the latter application, i.e., to have a null reflection around a frequency given by $k_0 = 1.39k_c$ (k_c being the cut-off frequency of the TE_{10} mode). Notice in Fig. 30 that the waveguide sections at the two ports are identical. Thus, if the two stubs were not present there would be no reflection (S_{11} ideally null) as the structure would simply consists of a waveguide section. The reason we analyze the structure in Fig. 30 (which has little practical application) is because this is a good test case. The idea is that for the null reflection frequency, the fields in the main waveguide have to be basically the same as those in a single waveguide section.
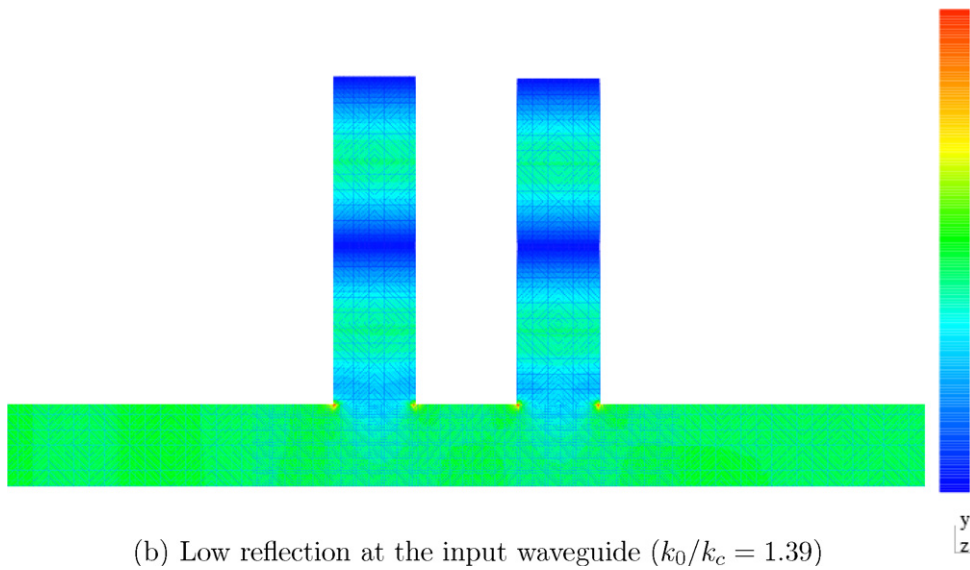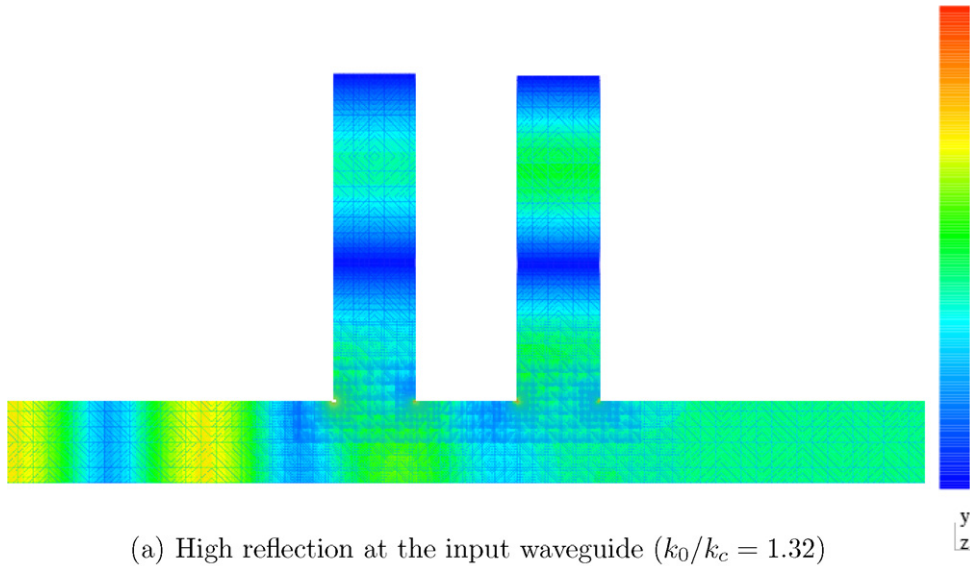
(a) High reflection at the input waveguide ($k_0/k_c = 1.32$)

(b) Low reflection at the input waveguide ($k_0/k_c = 1.39$)

Fig. 35. Electric field $\sqrt{|E_x|^2 + |E_y|^2}$ in the *E*-plane double stub section.

Since the stubs are identical, the structure is symmetrical ($S_{11} = S_{22}$). As in the other cases, the analysis is made by exciting port 1 (on the left).

The frequency response of the structure around the frequency corresponding to $k = 1.39k_c$ is shown in Fig. 31a. The ordinate axis corresponds to S_{11} in dB, i.e., $10\log_{10}|S_{11}|^2$ [14]. The results have been obtained by running the *hp*-adaptivity until an energy error of 1% is achieved

and computing S_{11} using the final *hp*-mesh. The expected low value of the reflection coefficient S_{11} around $k_0/k_c = 1.39$ is observed. For a comparison, Fig. 31 presents also results obtained using a MM technique. A very good agreement is observed.

Fig. 31b shows the frequency response over a broad frequency interval that consists of a centered band covering the 60% of the monomode frequency band. A very good agreement between the *hp*-FEM and MM results is observed. The only exception is around the frequency corresponding to $k_0/k_c = 1.74$. For these frequencies, a more refined mesh seems to be needed.

Convergence properties have been studied by executing the *hp*-adaptivity with an energy-norm error tolerance of 0.01% (and a maximum number of iterations equal to 20). Results corresponding to five significant frequency points (symmetrically chosen around the value of

---

[14] The dB is a logarithmic unit for dimensionless magnitudes, but it is always with respect to the power (and not the field) magnitudes. Thus, when applied to the scattering parameters that relate field quantities, the "10 $\log_{10}$" factor has to be applied to the square of the scattering coefficient. For example, $S_{11} = -40$ dB means that the power reflected at the input waveguide is 40 dB below the power of the excitation at the input waveguide, i.e., 10^4 lower (or equivalently, the electric and magnetic fields are 10^2 lower).

$k_0/k_c = 1.39$): $k_0/k_c = 1.32, 1.36, 1.42, 1.46$ are displayed in Fig. 32. For $k_0/k_c = 1.32, 1.46$ there is a high reflection of the energy at the input waveguide; for $k_0/k_c = 1.39$ there is a very low (almost null) reflection at the input; and for $k_0/k_c = 1.36, 1.42$ an intermediate situation occurs. Except for the first few iterations, the plots follow approximately a straight line, reflecting an exponential decrease of the energy-norm error. The erratic behavior of the error during the first few iterations is due to the coarseness of the initial mesh (shown in Fig. 33a).

The final meshes for $k_0/k_c = 1.32$ (high reflection at the input), $k_0/k_c = 1.39$ (low reflection at the input), and $k_0/k_c = 1.36$ (intermediate reflection at the input) are displayed in Figs. 33 and 34. For the case of high reflection, the mesh (shown in Fig. 33b) displays a typical refinement pattern around the corners (junctions of the stubs with the main waveguide). The electric field[15] for this case is plotted in Fig. 35a. A stationary wave pattern in the input waveguide is observed due to the interference between the incident and the reflected waves. On the other hand, the mesh for the low reflection case (shown in Fig. 34b) displays a situation very similar to the situation of the smooth field solution inside a waveguide section (i.e., without singularities). As it was explained above, this occurs because the stubs do not load the main waveguide (it is like if they were not present in the structure). This is best understood by seeing Fig. 35b, which displays the electric field in the structure for this case. The stationary wave pattern at the input waveguide can hardly be seen, which means that the level of the reflected wave is very low. Finally, the mesh for the intermediate case ($k_0/k_c = 1.36$) is shown in Fig. 34a. It is observed how effectively the mesh corresponds to an intermediate case between the meshes of Figs. 33 and 34b.

5. Conclusions

An *hp*-adaptive Finite Element Method for studying the characterization of microwave rectangular waveguide discontinuities with a geometry invariant along one direction (a common situation in rectangular waveguide technology), has been presented. The assumption on the geometry of the discontinuity enables a 2D analysis in the so-called *H*-plane or *E*-plane of the structure.

A fully automatic *hp*-adaptive strategy based on maximizing the rate of decrease of the (projection-based) interpolation error of the fine grid solution has been applied to a number of important engineering examples. Stabilized variational formulations for both *H*-plane and *E*-plane cases have been presented. Computation of the scattering matrix that characterize the electromagnetic behavior of the discontinuities for the microwave engineer has been implemented as a post-processing of the solution.

A wide variety of structures have been analyzed, including microwave engineering devices of medium complexity. The *hp* adaptivity has shown to deliver exponential convergence rates for the error for both regular and singular solutions. A consistent convergence pattern indicates that the results are more accurate than those obtained with semi-analytical techniques. At the same time, this *hp*-methodology presents the important advantage of being a purely numerical method, which allows for modeling complex waveguide structures that cannot be simulated using semi-analytical techniques.

References

[1] N. Marcuvitz, Waveguide Handbook, IEE, 1985.
[2] J. Uher, J. Bornemann, U. Rosenberg, Waveguide Components for Antenna Feed Systems: Theory and CAD, Artech House Publishers, Inc., 1993.
[3] L.F. Demkowicz, W. Rachowicz, P. Devloo, A fully automatic hp-adaptivity, J. Sci. Comput. 17 (1–3) (2002) 127–155.
[4] L. Demkowicz, Computing with *hp* finite elements. I. One- and two-dimensional elliptic and Maxwell problems, CRC Press, Taylor and Francis, 2006.
[5] W. Rachowicz, L.F. Demkowicz, An *hp*-adaptive finite element method for electromagnetics. Part 1: Data structure and constrained approximation, Comput. Methods Appl. Mech. Engrg. 187 (1–2) (2000) 307–337.
[6] L. Vardapetyan, L.F. Demkowicz, Full-wave analysis of dielectric waveguides at a given frequency, Math. Comput. 75 (2002) 105–129.
[7] L. Vardapetyan, L.F. Demkowicz, D. Neikirk, *hp* vector finite element method for eigenmode analysis of waveguides, Comput. Methods Appl. Mech. Engrg. 192 (1–2) (2003) 185–201.
[8] L. Vardapetyan, L. Demkowicz, *hp*-adaptive finite elements in electromagnetics, Comput. Methods Appl. Mech. Engrg. 169 (3–4) (1999) 331–344.
[9] W. Rachowicz, L.F. Demkowicz, A two-dimensional *hp*-adaptive finite element package for electromagnetics (2Dhp90_EM), Technical Report 16, Institute for Computational Engineering and Sciences, 1998.
[10] W. Rachowicz, L. Demkowicz, An *hp*-adaptive finite element method for electromagnetics. Part 2: A 3D implementation, Int. J. Numer. Methods Engrg. 53 (1) (2002) 147–180.
[11] L.F. Demkowicz, Fully automatic *hp*-adaptivity for Maxwell's equations, Comput. Methods Appl. Mech. Engrg. 194 (2–5) (2005) 605–624 (see also ICES Report 03-45).
[12] A. Wexler, Solution of waveguide discontinuities by modal analysis, IEEE Trans. Microwave Theory Tech. 15 (1967) 508–517.
[13] T. Itoh, Numerical Techniques for Microwave and Millimeter Wave Passive Structures, John Wiley & Sons, Inc., 1989.
[14] F. Ihlenburg, I. Babuška, Finite element solution of the Helmholtz equation with high wave number. I: The *h*-version of the FEM, Comput. Math. Appl. 30 (9) (1995) 9–37.
[15] F. Ihlenburg, I. Babuška, Finite element solution of the Helmholtz equation with high wave number. II: The *h*–*p*-version of the FEM, SIAM J. Numer. Anal. 34 (1) (1997) 315–358.

---

[15] Note that the magnitude plotted is $\sqrt{|E_x|^2 + |E_y|^2}$ that, although does not correspond to $|E|$ or other physically meaningful magnitude, it is useful for visualizing in one plot the field in the main waveguide and in the stubs.

[16] D. Pardo, L.E. García-Castillo, L.F. Demkowicz, A two-dimensional self-adaptive hp-adaptive finite element method for the characterization of waveguide discontinuities. Part II: Goal-oriented hp-adaptivity, Comput. Methods Appl. Mech. Engrg., in press, doi:10.1016/j.cma.2007.06.023.

[17] D. Pardo, L. Demkowicz, C. Torres-Verdin, L. Tabarovsky, A goal oriented hp-adaptive finite element method with electromagnetic applications. Part I: Electrostatics, Int. J. Numer. Methods Engrg. 65 (8) (2006) 1269–1309 (see also ICES Report 04-57).

[18] D. Pardo, L. Demkowicz, C. Torres-Verdin, M. Paszynski, Simulation of resistivity logging-while-drilling (LWD) measurements using a self-adaptive goal-oriented hp-finite element method, SIAM J. Appl. Math. 66 (6) (2006) 2085–2106.

[19] M. Paszynski, L. Demkowicz, D. Pardo, Verification of goal-oriented hp-adaptivity, Comput. Math. Appl. 50 (8–9) (2005) 1395–1404 (see also ICES Report 05-06).

[20] C.A. Balanis, Advanced Engineering Electromagnetics, John Wiley & Sons, Inc., 1989.

[21] R.F. Harrington, Time Harmonic Electromagnetic Fields, McGraw-Hill, Inc., 1961.

[22] R.E. Collin, Foundations for Microwave Engineering, second ed., McGraw-Hill, Inc., 1992.

[23] D.M. Pozar, Microwave Engineering, second ed., John Wiley & Sons, Inc., 1988.

[24] R.E. Collin, Field Theory of Guided Waves, IEEE Press, 1991.

[25] L.F. Demkowicz, Encyclopedia of Computational Mechanics, John Wiley & Sons, Inc., 2004 (Ch. Finite Element Methods for Maxwell Equations).

[26] J. Schwinger, D.S. Saxon, Discontinuities in Waveguides, Gordon and Breach, 1968.

[27] V.N. Kanellopoulos, J.P. Webb, A complete E-plane analysis of waveguide junctions using the finite element method, IEEE Trans. Microwave Theory Tech. 38 (1990) 290–295.

[28] K. Kurokawa, Power waves and the scattering matrix, IEEE Trans. Microwave Theory Tech. 13 (2) (1965) 194–202.

[29] W. Gui, I. Babuška, The h, p and h–p versions of the finite element method in 1 dimension – Part I. The error analysis of the p-version, Numer. Math. 49 (1986) 577–612.

[30] W. Gui, I. Babuška, The h, p and h–p versions of the finite element method in 1 dimension – Part II. The error analysis of the h- and h–p versions, Numer. Math. 49 (1986) 613–657.

[31] W. Gui, I. Babuška, The h, p and h–p versions of the finite element method in 1 dimension – Part III. The adaptive h–p version, Numer. Math. 49 (1986) 659–683.

[32] I. Babuška, B. Guo, Regularity of the solutions of elliptic problems with piecewise analytic data. Part I. Boundary value problems for linear elliptic equation of second order, SIAM J. Math. Anal. 19 (1) (1988) 172–203.

[33] I. Babuška, B. Guo, Regularity of the solution of elliptic problems with piecewise analytic data. II: The trace spaces and application to the boundary value problems with nonhomogeneous boundary conditions, SIAM J. Math. Anal. 20 (4) (1989) 763–781.

[34] I. Babuška, B. Guo, Approximation properties of the hp-version of the finite element method, Comput. Methods Appl. Mech. Engrg. 133 (1996) 319–346.

[35] C. Schwab, p- and hp- Finite Element Methods. Theory and Applications in Solid and Fluid Mechanics, Oxford University Press, 1998.

[36] W. Rachowicz, D. Pardo, L.F. Demkowicz, Fully automatic hp-adaptivity in three dimensions, Comput. Methods Appl. Mech. Engrg. 195 (37–40) (2006) 4186–4842.

[37] D. Pardo, L.F. Demkowicz, Integration of hp-adaptivity and multigrid. I. A two grid solver for hp finite elements, Comput. Methods Appl. Mech. Engrg. 195 (7–8) (2005) 674–710, see also ICES Report 02-33.

[38] D. Pardo, Integration of hp-adaptivity with a two grid solver: applications to electromagnetics, Ph.D. thesis, University of Texas at Austin, 2004.

[39] L.F. Demkowicz, P. Monk, L. Vardapetyan, W. Rachowicz, De Rham diagram for hp finite element spaces, Comput. Math. Appl. 39 (7–8) (2000) 29–38.

[40] L.F. Demkowicz, I. Babuška, Optimal p interpolation error estimates for edge finite elements of variable order in 2D, SIAM J. Numer. Anal. 41 (4) (2003) 1195–1208.

[41] L.F. Demkowicz, A. Buffa, H^1, H(curl) and H(div)-conforming projection based interpolation in three dimensions. Quasi optimal p-interpolation estimates, Comput. Methods Appl. Mech. Engrg. 194 (24) (2005) 267–296 (see also ICES Report 04-24).

[42] L.F. Demkowicz, Projection-based interpolation, no. 03, Cracow University of Technology Publications, Cracow, 2004, monograph 302, A special issue in honor of 70th Birthday of Prof. Gwidon Szefer, see also ICES Report 04-03.